Understanding Atomic-Scale Mechanisms of Adhesion and Deformation at Contacting Surfaces: Quantitative Investigations Using *In situ* TEM

by

Sai Bharadwaj Vishnubhotla

Bachelor of Technology in Metallurgical and Materials Science Engineering, Visvesvaraya National Institute of Technology, 2013

Master of Science in Materials Science and Engineering, Stony Brook University, 2015

Submitted to the Graduate Faculty of the

Swanson School of Engineering in partial fulfillment

of the requirements for the degree of

Doctor of Philosophy

University of Pittsburgh

2020

UNIVERSITY OF PITTSBURGH

SWANSON SCHOOL OF ENGINEERING

This dissertation was presented

by

Sai Bharadwaj Vishnubhotla

It was defended on

March 13, 2020

and approved by

Jörg Wiezorek, Ph.D., Professor, Department of Mechanical Engineering and Materials Science

Scott Mao, Ph.D., John Swanson Professor, Department of Mechanical Engineering and Materials Science

Götz Veser, Ph.D., Nickolas A. DeCecco Professor, Department of Chemical and Petroleum Engineering

Dissertation Director: Tevis Jacobs, Ph.D., Assistant Professor, Department of Mechanical Engineering and Materials Science

Understanding Atomic-Scale Mechanisms of Adhesion and Deformation at Contacting Surfaces: Quantitative Investigations Using *In situ* TEM

Sai Bharadwaj Vishnubhotla, PhD

University of Pittsburgh, 2020

Nanoscale contacts are relevant in advanced technologies like nanomanufacturing, scanning probe microscopy, micro- and nanoelectromechanical systems, nanodevices, and nanostructured catalysts. In all cases, functional properties such as adhesion, friction, electrical, and thermal transport depend on the size and nature of the contact. Continuum-based contact mechanics models are routinely applied to describe the behavior of these contacts in real-world applications, despite evidence of breakdown of their underlying assumptions at the nanoscale. In order to understand the applicability of contact mechanics at the nanoscale, and also the nature of any observed deviations, the present dissertation research uses *in situ* transmission electron microscopy (TEM) experiments and matched molecular dynamics (MD) simulations to perform loading and adhesion tests on nanoscale contacts. Specifically, the true contact area at varying loads is measured in experiment and atomistic simulation and compared against the predictions of continuum models for three different classes of materials: noble metals, covalently bonded materials, and metal oxides.

First, for noble-metal contacts, it is observed that direct measurements of contact radius exceed the predictions of contact mechanics due to dislocation activity in the near-surface material, which is fully reversed upon unloading. Second, for same contacts, electron transport models under-predict the contact size by more than an order of magnitude. It is due to a robust monolayer of surface species on the contact interface, and the contact size is predicted better with tunneling theory. Third, for silicon-diamond contacts, the work of adhesion increases with applied stress

which is contrary to the underlying continuum assumption that adhesion energy is a constant for a given material system. Such behavior is also observed for self-mated contacts of titania. This suggests that, for covalently bonded systems, the loading modifies the atomic-scale interactions at the interface and increases the adhesion strength. The primary implications of the present dissertation are two-fold: first, these findings demonstrated that commonly-used contact mechanics models are insufficient in predicting the contact properties in real-world nanostructures, and suggest modifications to account for atomic-scale phenomena; and second, these findings reveal the different physical mechanisms that govern the contact behavior of metals and covalent solids.

Table of Contents

List of Figures

Preface

I wish to thank my advisor Prof. Tevis Jacobs for his inspiration, guidance, and for providing numerous opportunities for professional development during my PhD.

I wish to thank Prof. Jörg Wiezorek, Prof. Scott Mao, and Prof. Götz Veser for serving on my PhD committee and providing scientific support along the way.

I am grateful for the continued support and discussions with our collaborators Rimei Chen, Dr. Xiaoli Hu, and Prof. Ashlie Martini at the University of California, Merced.

I wish to thank Dr. Jing Li and Prof. Eric A Stach for their help in using the resources of the Center for Functional Nanomaterials at Brookhaven National Laboratory where a part of the study discussed in Chapter 5 was conducted.

I wish to thank Nic Argibay (Sandia National Lab), Evgheni Strelcov (NIST), and Maarten de Boer (CMU) for their helpful scientific discussions on Chapter 5.

I wish to thank Ryan Major (Bruker), Sanjit Bhowmick (Bruker), and Daan Hein Alsem (Hummingbird Scientific) for their technical support on in situ TEM holders.

I wish to thank Dr. Subarna Khanal for support on TEM work. I wish to thank Dr. Yahui Yang and Sanjana Karpe for their support with nanoparticle synthesis. I wish to thank Andrew Baker for his help in the data analysis for Chapter 7.

I wish to thank the current and former members of Jacobs research group for their support, guidance, assistance, and fun.

Finally, I wish to thank my family and friends for their unconditional support and love.

Use of facilities of the Nanoscale Fabrication and Characterization Facility (NFCF) in the Petersen Institute of NanoScience and Engineering at the University of Pittsburgh is

acknowledged. Also, funding from the National Science Foundation (Grants CMMI-1536800) is gratefully acknowledged.

1.0 Motivation for the Study of Mechanical and Electrical Properties of Nanoscale Contacts

As devices and manufacturing technologies shrink to the nanoscale, there is a growing need to understand, predict, and control the behavior of small-scale contacting interfaces. Examples of this need stem from nanomanufacturing, materials characterization, and nanodevices. Specifically, in tip-based nanomanufacturing [1, 2], probe-based lithography [3], and in micro-transfer printing of quantum dots [4], the behavior of the nanocontact determines reliability and precision. In the vast array of techniques of scanning probe microscopy (SPM) – such as conductive atomic force microscopy (c-AFM) [5, 6], scanning spreading resistance microscopy [7, 8], scanning capacitance microscopy [9], and scanning nano-thermometry [10] – the contact's size and properties determine both the resolution of the technique and the accuracy of models applied for quantitative analysis. In both c-AFM [5] and nanodevices [11], the current flow through these nanocontacts depends not only on the material properties of the contacting bodies, such as resistivity and carrier density, but also on the true area of the contact. Finally, in these nanodevices such as switches and actuators [11, 12], the mechanical and transport properties of the contact determine functionality and lifetime of the device. Hence, these advanced applications require a comprehensive and predictive understanding of behavior as the nanocontact forms, evolves, and separates, which is the topic of the present dissertation.

2.0 Adhesion, Deformation, and Conductance of Nanoscale Contacts−A Review

2.1 Review of Contact Mechanics Models

A model to describe the mechanical properties of contacting bodies was first derived by Heinrich Hertz [13] that relates deformation and contact area to the applied load for two contacting elastic spheres without adhesion. The Hertz model relates contact radius a_{Hertz} and deformation δ_{Hertz} to applied force F_{app} as follows:

$$a_{Hertz} = \left(\frac{3RF_{app}}{4E^*}\right)^{1/3} \tag{2-1}$$

$$\delta_{Hertz} = \left(\frac{9F_{app}^2}{16RE^{*2}}\right)^{1/3} \tag{2-2}$$

where R is the asperity radius against a flat surface, and E^* is the effective modulus. The effective modulus is defined for a contact as $E^* = \left[\frac{(1-\upsilon_1^2)}{E_1} + \frac{(1-\upsilon_2^2)}{E_2}\right]^{-1}$, where E is the Young's modulus and ν is the Poisson ratio and the subscripts 1,2 designate the two different materials in contact. The assumptions of this model are: (i) the two bodies in contact are homogenous and isotropic, (ii) the surfaces are smooth and frictionless, and (iii) the contact radii a_{Hertz} and elastic deformation δ_{Hertz} are much smaller than the size of the contact bodies.

Adhesion is always present between contacting surfaces and the two factors governing adhesion are the fundamental physical interactions between the materials and the geometry (global and local) of the surfaces in contact. The first factor which is physical interactions includes the

atomic-scale interactions such as van der Waals attraction, electrostatic interactions, and atomic bonding and is described by the work of adhesion W_{adh}, which is the energy required per unit area to separate flat surfaces of the two materials from equilibrium separation to infinity [14]. In terms of surface energy of the two materials γ_1 and γ_2, and interfacial energy γ_{12} the work of adhesion is defined as [14]:

$$W_{adh} = \gamma_1 + \gamma_2 - \gamma_{12} \tag{2-3}$$

For a self-mated contact the $W_{adh} = 2\gamma$. The second factor governing adhesion is the effect of the geometry of the contacting surfaces. First, Bradley [15] demonstrated the effect of geometry on adhesion when he showed that the adhesive force F_{adh} between a rigid sphere of radius R and a rigid flat surface of the same material is described as $F_{adh} = 2\pi R W_{adh}$. Later Derjaguin [16] approximated the adhesive force which is the same as that of Bradley and along with co-workers established the Derjaguin–Müller–Toporov (DMT) model [16]. The DMT model is an extension to the Hertz model to account for the adhesion between the bodies. The contact radius as a function of force for the DMT model is obtained by replacing the F_{app} in the Hertz model (Eq. 2-1 and 2-2) by $F_{total} = F_{app} + F_{adh}$ as follows [16]:

$$a_{DMT} = \left(\frac{3RF_{total}}{4E^*}\right)^{1/3} \tag{2-4}$$

$$\delta_{DMT} = \left(\frac{9F_{total}^2}{16RE^{*2}}\right)^{1/3} \tag{2-5}$$

The DMT model assumes weaker and longer-range adhesive interactions and is applicable for stiffer materials. The characteristics of the DMT model is that the contact size goes to zero at the adhesive force F_{adh} and the stresses in the contact are maximum at the center and go to zero at the edge of the contact.

Several years later to the Bradley model, Johnson, Kendall, and Roberts (JKR) [17] introduced an elastic adhesive model that assumes stronger and shorter-range adhesion causing contact area to increase more than that is predicted by the DMT model. The adhesive force for the JKR model is given by $F_{adh} = 1.5\pi R W_{adh}$. The contact radius and deformation of the contact bodies are given by [17]:

$$a_{JKR} = \left[\frac{3R}{4E^*}\left(F_{app} + 2F_{adh} + \sqrt{4F_{app}F_{adh} + 4F_{adh}^2}\right)\right]^{1/3} \tag{2-6}$$

$$\delta_{JKR} = \frac{a_{JKR}^2}{R} - \left(\frac{2\pi W_{adh} a_{JKR}}{E^*}\right)^{1/2} \tag{2-7}$$

The characteristics of the JKR model are: (i) it is applicable for compliant materials, (ii) the contact size is non-zero at the adhesive force, and (iii) the stresses closer to the edge of the contact are tensile and reaches singularity on the edge of the contact.

These models are useful to predict the contact properties such as contact area, deformation, and work of adhesion. However, for the two materials in contact, different values can be obtained depending on the applied model. This dispute was first clarified by Tabor [18] who proposed that the DMT and JKR models are the two different limits of the adhesive contact behavior and the

cases between them can be quantified using a dimensionless transition parameter known as Tabor parameter μ_T given by [18]:

$$\mu_T = \left(\frac{RW_{adh}^2}{E^{*2}z_0^3}\right)^{1/3} \tag{2-8}$$

where z_0 is the equilibrium separation between the materials. The transition parameter is the ratio of elastic deformation to the length-scale of surface forces. Later Maugis [19] proved that DMT and JKR are the limits of the spectrum and also provided the equations to predict the contact properties for the intermediate cases between the limits. All the cases are described by the Maugis-Dugdale model [19] in which the interaction potential between the contact bodies was approximated by a 'Dugdale' (square-well) potential, where an adhesive stress σ_0 acts over a range of adhesion h. The adhesive stress σ_0 is determined by equating it to the minimum adhesive stress of the Lennard-Jones potential, which gives $\sigma_0 = W_{adh}/0.97z_0$ [20]. These intermediate cases are defined by a dimensionless parameter known as transition parameter λ which is calculated as [19]:

$$\lambda = 2\sigma_0 \left(\frac{9R}{16\pi E^{*2} W_{adh}}\right)^{1/3} \tag{2-9}$$

This transition parameter λ is equivalent to μ_T related by $\lambda = 1.157\mu_T$. The transition parameter is used to describe the intermediate cases between the DMT and JKR limits and the contact area and deformation as a function of force is provided by the Maugis-Dugdale model [19]. These equations are difficult to implement directly and were simplified by Carpick *et al.* [20] to

present a numerical analysis for determining the contact area as a function of force for the intermediate cases. Similar numerical analysis was extended for determining deformation for the intermediate cases [21]. Using the complete picture of the contact behavior provided by the Maugis-Dugdale model [19], the work of adhesion W_{adh} is calculated as follows [20]:

$$W_{adh} = \frac{F_{adh}}{\chi \pi R} \tag{2-10}$$

where χ is a constant that is equal to 1.5 for the JKR model [17], 2 for the DMT model [16], and an intermediate value for the Maugis-Dugdale model [19].

In order to determine which contact model should be applied to a given contact, the method described in Ref. [22] is used to calculate the range of Tabor parameter μ_T. The equilibrium separation z_0 is not directly measurable and a range of values is assumed for the given pair of materials [22]. The upper bound of the μ_T is calculated using Eq. 2-8 with the lower bound value of z_0 and W_{adh} determined by JKR. The lower bound of the μ_T is calculated using Eq. 2-8 with the upper bound value of z_0 and W_{adh} determined by DMT. If the determined range of μ_T is less than 0.1, then a DMT limit should be applied and for μ_T greater than 5, JKR limit should be applied. For all the values between 0.1 and 5, intermediate cases described by Maugis-Dugdale model should be applied. By following the procedure above, the contact area, deformation, and work of adhesion can be calculated for the contact.

The geometry of the single asperity on the end of the AFM probe has been shown to change from approximately spherical to either completely flat, and a large range of such shapes has been shown to be well-described using an analytical function: an axisymmetric power-law [23]. Thus, the spherical contact mechanics models described previously (Hertz, DMT, JKR, Maugis models)

have been extended for such non-spherical geometries [24, 25] where the 3D shape can be described by an analytical power-law function, $z(r) = r^n/nQ$, where *r* is the radial distance, *n* is power index, and *Q* describes the curvature of the probe profile. The Maugis-Dugdale type of model analysis (referred to as M-D-*n* model [24]) was used to describe the contact properties for the geometries described by the power-law function. For the JKR-limit of the M-D-*n* model (referred to as JKR-*n*), the relationship between the contact radius and force is described by [24]:

$$\bar{F}_{app} = \frac{1}{\pi}\mathbf{B}\left(\frac{n}{2}+1,\frac{1}{2}\right)\bar{a}^{n+1} - \frac{2}{\pi}\sqrt{2\pi\bar{a}^3} \tag{2-11a}$$

where **B** is the Euler beta function, $\bar{F}_{app}$ is dimensionless force and $\bar{a}$ is dimensionless contact radius. And the DMT-limit of the power-law model (DMT-n) is described by [24]:

$$\bar{F}_{app} = \frac{1}{\pi}\mathbf{B}\left(\frac{1}{n}+1,\frac{1}{2}\right)\bar{a}^{n+1} - n^{2/n}\Lambda^{(n-2)/n} \tag{2-11b}$$

where Λ is the dimensionless transition parameter. The dimensionless force and contact radius can be expressed in terms of applied force F_{app} and contact radius *a* as follows [24]:

$$\bar{F}_{app} = F_{app}\ /\pi(Q^3 W_{adh}^{n+1} E^{*n-2})^{1/(2n-1)} \tag{2-11c}$$

$$\bar{a} = a/(Q^2 W_{adh} E^{*-1})^{1/(2n-1)} \tag{2-11d}$$

For n = 2, the power-law function describes a parabolic shape and by substituting n = 2 in the Eq. 2-11(a-d), it gives the equations as described by the Maugis-Dugdale model [19]. Though similar analysis of spherical contact models can be used for $n > 2$, the adhesive force F_{adh} not only depends on the work of adhesion W_{adh} but also on the range of adhesion h. Thus, it becomes difficult to extract the W_{adh} as the range of adhesion is usually unknown [23, 24].

In summary, the field of contact mechanics (a sub-field of solid mechanics) has developed a wide array of models to analytically or numerically describe the behavior of bodies in contact. The key variables in these models include material parameters (E^*, ν, W_{adh}) and the shape of the bodies in contact (spherical, flat-punch-like, or described by a power-law function). Using these key variables, the contact mechanics models can be used to predict the contact properties such as contact size, deformation, stresses, and adhesion.

2.2 Prior Applications of Contact Mechanics Models to Nanoscale contacts

For technologically relevant nanoscale contacts (of the type described in Sect. 1), it is common to predict the nanoscale contact area using these continuum mechanics models (Sect. 2.1) due to their ease of use and closed-form predictions for contact radius [26]. These continuum models and their various extensions rely on underlying assumptions (such as perfectly smooth surfaces, small deformation compared to the size of the body, and isotropic materials) that may be violated at nanometer length scales. Numerous experimental investigations using SPM have been used to test the applicability of contact mechanics models. In SPM, the contact area cannot be directly visualized. Thus, the contact area is calculated indirectly by measuring electrical current [27] or friction force [28]. In these approaches, the ballistic regime [29] is assumed which predicts

that the contact area is proportional to electrical current. Similarly, the measurement of friction force $F_{friction}$ gives a direct measure of contact area $A_{contact}$ under the assumption that $F_{friction} = \tau A_{contact}$, where τ is the interfacial shear strength. Using these approaches, it was shown that the spherical contact models *are* applicable even down to the nanoscale [27, 30, 31]. Similar support of applicability is also shown for power-law contact models where in some cases TEM imaging of the SPM probe was used to confirm the power-law geometry [23, 25, 32]. However other SPM-based investigations suggest the breakdown of the applicability for these models [33–35], specifically due to surface roughness, plastic deformation, and in some cases due to pressure dependence of interfacial shear strength [33, 34].

An alternative to continuum models is atomistic simulations, which are able to track the position of each atom and have been employed to study nanocontacts mimicking experimental conditions [36–40]. Some such simulations have suggested that contact mechanics may be applied when atomic-scale surface roughness is considered in the model [41] or for modifications of the theories, such as thin-coating contact mechanics [37, 42]. However, other studies showed that continuum contact mechanics may break down due to atomic-scale roughness [43–47]. Further, due to the discreteness of atoms at the contact interface, the definition of contact is ambiguous at the atomic scale, which complicates comparison between atomistic models and continuum mechanics predictions [41, 48, 49]. Moreover, while simulation investigations [41, 43, 44, 48] suggest that the discreteness at atomic-scale and nanoscale roughness will cause significant deviations in the spatial distribution of surface pressure and the measured friction force, they do not predict meaningful deviations in contact radius and are shown to agree with continuum predictions within a few percent [43, 44].

In summary, despite extensive investigation of the topic, the field was still lacking in direct evidence to support or refute the applicability of the contact mechanics models at the nanoscale. The field also lacks guidelines under which these models would be applicable for a particular material, load or geometry. Further, additional information is required regarding the shape and structure of the contact interface. Hence, it remains unclear whether the contact mechanics models can be applied at the nanoscale to accurately predict the contact properties.

2.3 Experimental Measurements of Mechanical Properties for Nanoscale Metal Contacts

Understanding of single-asperity metal contacts requires an understanding of both the elastic and inelastic deformation of the metals and the contact behavior of metallic interfaces. Extensive work has been conducted using micro-compression and tensile testing to study the size-dependence of the yield strength on pillar-like structures of single crystals of FCC metals (Cu[50], Al [51], Au [52], Ni [53]) and BCC metals (Mo [54]). These studies have shown that the strength of the material increases with the decrease in the sample dimensions (detailed review is provided in Ref. [55]). Other SPM-based nanoindentation experiments on Au [56] and Cu [57] have studied the load-deformation behavior to correlate the onset of plasticity in these metals with the creation and movement of dislocations. The aforementioned studies provide the understanding of the inelastic behavior of the metals over the sample dimensions of micron to nanometer range. However, there is a lack in understanding of the inelastic behavior at size scales below 100 nm [58].

Notable exceptions where the inelastic deformation of sub-100 nm size structures have been well studied are noble metal nanojunctions of Au [59, 60] and Ag [61, 62]. Gold is known to

exhibit “cold-welding” which is spontaneous formation of a neck between the two bodies, and liquid-like shape change, including necking down to a thin junction of atoms before breaking [63]. This cold welding takes place when two nanometer-size gold bodies come into contact, which has been directly observed using *in situ* TEM [64–67] and MD simulations [68]. *In situ* TEM investigation by S. X. Mao and coworkers [60] have shown that the elongation or thinning down of gold nanojunction takes place with discrete plasticity events in which partial dislocations are emitted by the free surfaces. By contrast, *in situ* TEM study of the deformation of silver nanometer-size junctions show no dislocation activity; rather, it has been described [61] as a surface-diffusion-mediated rearrangement process. In both of these cases, the two contacts fuse together and the original interface is lost. Therefore, their behavior is governed by material rearrangement under tensile stress and therefore is not governed by continuum mechanics. In separate experiments, Cross *et al* [69] conducted nanoindentation of gold at cryogenic temperatures (which suppressed the liquid-like behavior that is seen by others [59]) in ultra-high vacuum (UHV) to show that dislocation plasticity can play a significant role in metallic contacts, and that it can act reversibly. This plasticity-mediated reversible deformation is expected to cause deviations from the predictions of continuum elasticity; however, these nanoindentation experiments were carried out at higher applied loads (>100 nN) and lower temperatures (-123 °C) than are typically experienced by nanocontacts in technological applications. Therefore, it remains unclear how dislocation activity may affect the contact behavior of applications-relevant metallic nanocontacts under adhesive-only loads.

The prediction of the contact properties such as contact size and adhesion using elastic contact mechanics models for metals at the nanoscale is not clear. These models assume homogeneity, isotropic, linear elasticity, and size of contact bodies much greater than contact

radius which could breakdown at the nanoscale. The SPM-based investigation by Lantz *et al* [27] for a conductive contact using platinum-coated SPM tip suggests that the contact behavior can be far from ideal elastic contact due to wear of the metal asperity, contamination films on the surface, and plastic deformation due to high stresses in the contact interface. Bennewitz and coworkers [70–74] have extensively studied friction in metal nanocontacts of gold, copper, and platinum. For the single crystal surfaces of gold [71] and copper [73], they have observed ultra-low friction under very low loads. The physical mechanism for the ultra-low friction was suggested to be due to the formation of the neck between the SPM tip and surface by diffusion, and the neck remains intact even during the sliding [70–73]. The contact size, current, and adhesion of such a nanocontact are entirely determined by the neck, not by contact mechanics models.

In summary, excellent prior investigations using experiments and simulations provide insights into the inelastic deformation behavior of sub-100 nm metallic structures. However, most of the studies have been conducted on homogenous metallic junctions rather than on a well-defined interface. Hence, it remains unclear how dislocation activity, plastic deformation, and cold welding may affect the contact behavior of metallic nanocontacts under low and adhesive loads.

2.4 Review of Electron Transport Models for Metallic Contacts

Electron transport models provide an indirect measure of the contact size by measuring the current through the conductive contact interfaces [75]. Holm showed that contact resistance for a metallic junction is due to the flow of current through a constriction of small area often known as the "a-Spot" model [75]. In late 1930, Bowden and Tabor [76] used this method to show that true area of contact between two rough metal surfaces is less than the apparent contact. Electron

transport through a homogenous metallic contact with no oxide or contamination is modeled as a function of the circular constriction radius a and the mean free path of an electron l_f in the material. Specifically, the behavior is described using diffusive (Maxwell), ballistic (Sharvin), and intermediate (Wexler) theories of electron transport [75]. When the contact radius is much larger than the mean free path of the electron, the electrical conductance is given by [75]:

$$G_D = \frac{2a}{\rho} \tag{2-12a}$$

where ρ is the resistivity of the metal. When the contact radius is smaller than the mean free path length, the electrical conductance is described by the ballistic theory formulated by Sharvin as [29]:

$$G_B = \frac{3\pi a^2}{4\rho l_f} \tag{2-12b}$$

When the contact radius is approximately equal to the mean free path length, the electrical conductance is given by the intermediate theory as [77]:

$$G_I = \left[\Gamma(K)\left(\frac{1}{G_M}\right) + \left(\frac{1}{G_S}\right)\right]^{-1} \tag{2-12c}$$

where $K = l_f / a$ is the Knudsen number, and Γ(K) is a slowly varying function from 1 to 0.694 [77]. A simplified version of Γ was provided by Nikolic and Allen [78], such that the intermediate conductance can be rewritten as [78]:

$$G_I = \left[\left(\frac{1+0.83(l_f/a)}{1+1.33(l_f/a)}\right)\left(\frac{1}{G_D}\right) + \left(\frac{1}{G_B}\right)\right]^{-1} \quad (2\text{-}13)$$

2.5 Experimental Measurements of Electron transport for Metallic Contacts[1]

Metallic nanocontacts are ubiquitous in existing and emerging technologies such as c-AFM [3, 79] and electromechanical switches [11]. For these applications, the contact area is indirectly measured by measuring the current flow and applying electron transport theories [27, 80]. In these advanced applications, the contact size is small, and the radius of contact is typically smaller than or comparable to the mean free path (4 to 50 nm for most metals [75]). Hence, it is very common to predict the electrical current through contact using ballistic or intermediate theory.

[1] Much of this section appears in print: Adapted with permission from Vishnubhotla, S.B., Chen, R., Khanal, S.R., Li, J., Stach, E.A., Martini, A., Jacobs, T.D.B.: Quantitative measurement of contact area and electron transport across platinum nanocontacts for scanning probe microscopy and electrical nanodevices. Nanotechnology. 30, 45705 (2019). Copyright © 2018 IOP Publishing Ltd.

Numerous investigations over the last two decades have applied the electron transport theories to metal nanocontacts. For example, several studies have used these theories to measure the size of the tip/sample contact in c-AFM [27, 28, 30]. More recently, a combined c-AFM and simulation investigation used the ballistic model to describe electron transport through a conductive doped ultrananocrystalline diamond tip and a graphene sheet [81]. Further, various analytical models have been proposed to describe electron transport through technologically relevant devices such as microelectromechanical systems (MEMS) switches [82–91]. These models describe microcontacts, which have inherent roughness, as an array of smaller point-contacts, each of which is described by the intermediate transport theory. These transport theories are also used in first-principles calculations for modelling electrical resistance for copper interconnects [92]. Finally, recent electrical characterization of metal nanostructures have suggested the applicability of the ballistic theory to describe electron transport in silver nanowires [93]. These examples represent a small sampling of the broad application of transport theories to metal nanocontacts in a wide range of advanced technologies.

However, some investigations suggest the failure of electron transport theories to describe transport through nanocontacts, even for noble metals. *In situ* TEM investigation on gold nanocontacts [94] showed lower conductance than expected from an intermediate theory. Other nanoindentation measurements combined with MD simulations of a tungsten/gold contact also showed lower conductance than expected using ballistic theory [95]. These studies suggested that the observed behavior is caused mainly due to significant scattering by the defects at the interface [94, 95]. Furthermore, experimental investigation [96] of single-asperity platinum contacts using atomic force microscopy has suggested the formation of an insulating tribopolymer layer after billions of loading/unloading cycles. Additionally, atomistic simulations have suggested a

significant decrease in conductance with just a 0.36-nm thick layer of adsorbates [97]. Density functional theory (DFT) simulations [98] have indicated that platinum contacts can form carbonaceous surface layers under the action of mechanical stress and voltage.

In summary, significant work has been conducted to understand the electron transport across single-asperity contacts; however, there is still a lack of quantitative understanding of the relationship between contact radius and current flow for nanoscale bodies in contact.

2.6 Concluding Remarks Regarding the Understanding and Prediction of Contact Properties for Nanoscale Contacts

All the above studies suggest a need for quantitative understanding of the contact properties such as contact size, adhesion and current flow for nanoscale contacts. Scanning probe microscopy investigations on understanding the applicability of contact mechanics models have significantly advanced our understanding, but the contact properties can only be determined indirectly using contact models. Therefore, they do not provide a direct method to verify the applicability of those models. TEM-based investigations provide a quantitative measure of the geometry and structure of the bodies. Excellent prior investigations have examined homogenous metallic junctions with no interface; however, these do not provide insights into contacts that maintain a defined interface, as most nanoscale contacts do. Also, it is not clear how dislocations affect the contact properties for such metal contacts. Atomistic simulations provide direct visualization of the contact interface with load measurement, but it is impractical to rely on simulations in every contact situation because they are typically time-and resource-intensive. As such, there is benefit to having analytical expressions from contact mechanics models, even if they are approximate. Also in

simulations, there are several methods to define the contact which leads to different measurement of the contact size depending on the methods used [48, 99] which makes it difficult to validate the contact mechanics predictions. Overall, it is not known whether the contact mechanics models are applicable at the nanoscale. If the models fail, what are the physical mechanisms that cause these deviations for nanoscale contacts? Significant work has been done on understanding the electron transport for metal nanocontacts, but there is a lack in quantitative relationship between contact size and current and how it is affected by the oxide or contamination films.

Answering these critical questions will have a significant impact on nano-manufacturing, probe-based lithography, MEMS, and nanodevices as many of these techniques still rely on contact mechanics and electron transport models. The performance, accuracy, and reliability of these applications rely on the accurate measurement of the contact size and adhesion. It will also have an impact on probe-based materials characterization techniques where the precise determination of functional properties depends on the accurate measurement of the contact size.

3.0 Measurement of Contact Properties for Nanoscale Contacts Using *In situ* TEM

3.1 Measurement of the Applied and Adhesive Forces from *In situ* TEM Tests[2]

In this investigation, loading and adhesion tests were performed on a nanoscale contact inside of a transmission electron microscope. This was done using an *in situ* TEM nanoindentation holder (Hysitron PI 95, Bruker, Billerica, MA) in a TEM (2100F, JEOL, Tokyo, Japan) that was operating at an accelerating voltage of 200 kV (Fig. 1a). Unlike traditional nanoindentation, an AFM probe with a nanoscale apex was mounted in place of the sample and was contacted by a flat-punch diamond indenter. The AFM chip body was cleaved and glued to the sample mount of the nanoindenter. Commercial silicon AFM probes were used (PPP-NCLR, NCHR, FMR Nanosensors, Neuchatel, Switzerland), which had initial apex radii of approximately 5 nm and contained an oxide from the manufacturing process that extended to a height of approximately 10-15 nm at the apex. This oxide was mechanically removed by bringing the indenter into contact with the probe and sliding it in vacuum prior to testing. After removing the oxide, the silicon crystal lattice was observed to extend to the apex of the probe (Fig. 1a). Before testing, the diamond indenter was cleaned with light mechanical abrasion using a cotton swab and acetone. Next, the indenter was sequentially ultrasonicated in isopropanol, acetone, and methanol. This cleaning procedure was recommended by the manufacturer for nanoindenters, and has been used in prior

[2] Much of this section appears in print: Adapted with permission from Chen, R.*, Vishnubhotla, S.B.*, Khanal, S.R., Jacobs, T.D.B., Martini, A.: Quantifying the pressure-dependence of work of adhesion in silicon-diamond contacts. Appl. Phys. Lett. 116, 051602 (2020). Copyright © 2020, AIP Publishing. *Indicates equal contribution.

studies [100, 101]. Further, direct inspection using the TEM verified that there was no significant debris or contamination on the surface. This direct inspection was also used to rule out the possibility of carbonaceous contamination during imaging. While the build-up of carbonaceous contamination has been observed in electron microscopy [102], this is most problematic for very high electron doses and/or poor vacuum in the chamber. It was not observed in the present study, even after significant additional beam exposure after completion of the test.

High-resolution TEM imaging was used to determine the geometry and crystal orientation of the tip apex of the probes. The real-time video enabled the characterization of instantaneous contact radius a, after correcting for the vibration of the instrument. The instantaneous applied force was determined with nanonewton resolution using either or both of two ways: for forces larger than 200 nN, the on-board 3-plate-capacitor load cell was used for direct measurement (Fig. 1b); for forces smaller than 200 nN, the deflection of the cantilever (measured from the TEM video) was multiplied by the pre-calibrated [103] spring constant k to determine the load (Fig. 1c). This is the general established procedure to conduct *in situ* TEM contact tests on different material systems.

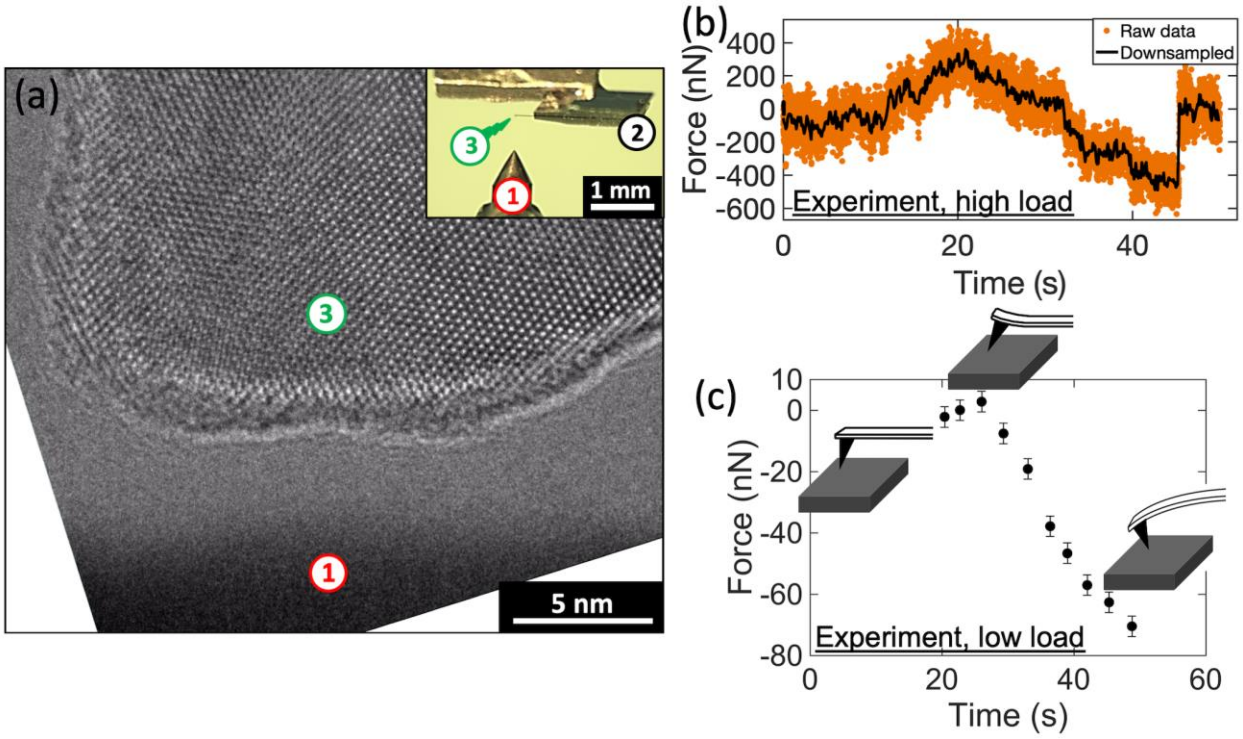

Figure 1. The adhesion tests were performed using *in situ* TEM experiments. *In situ* TEM adhesion tests (a) were performed between a flat nanoindenter (1, inset) and an AFM probe (2,3, inset). Forces were measured using either the nanoindenter's load sensor (b) or the deflection of the calibrated cantilever (c). Figure reproduced with permission from Ref. [104].

3.2 Measurement of the Conductance for Noble Metal Contacts Using *In situ* TEM Tests[3]

Experimental electromechanical contact tests were conducted on self-mated platinum nanocontacts using the procedure as described in the Sect. 3.1. Platinum-coated AFM probes (*Electri*Multi75-G PFM, BudgetSensors, Sofia, Bulgaria) were bonded to the sample mount of the indenter. The indenter is comprised of a platinum wire (99.9% pure, Sigma-Aldrich, St. Louis, Missouri, USA) which was mechanically sharpened and placed in the indenter mount. Prior to testing, the AFM probes were rubbed against the substrate in a remote location to remove any adsorbed contamination. Then the probes were brought into contact with the substrate, loaded to maximum force, and unloaded to the point of pull-off with a speed of 1.5 nm/s (as shown in Fig. 2a). During the loading and unloading cycles, current-voltage (I-V) sweeps were collected at various applied forces. In all cases comprising of platinum contacts, the current varied linearly with voltage indicating Ohmic behavior, and the conductance was calculated from the slope of the I-V curve, $G = dI/dV$ (Fig. 2b).

[3] Much of this section appears in print: Adapted with permission from Vishnubhotla, S.B., Chen, R., Khanal, S.R., Li, J., Stach, E.A., Martini, A., Jacobs, T.D.B.: Quantitative measurement of contact area and electron transport across platinum nanocontacts for scanning probe microscopy and electrical nanodevices. Nanotechnology. 30, 45705 (2019).

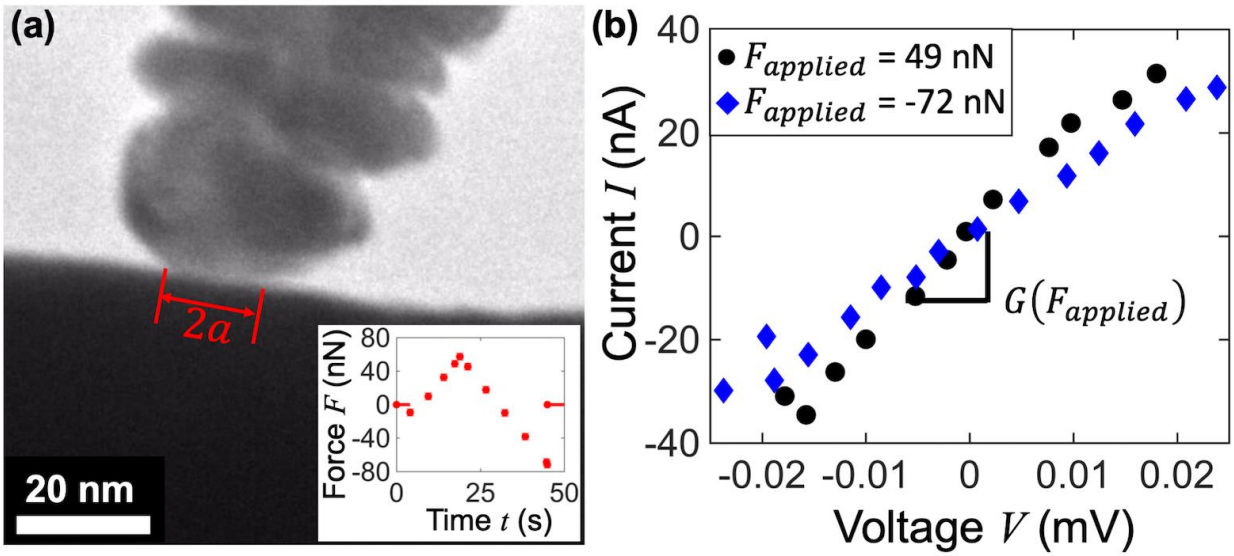

Figure 2. *In situ* electromechanical contact testing was performed inside of a transmission electron microscope. A flat platinum indenter is brought into contact with a platinum-coated AFM chip, such that it can be brought into contact with the nanoscale apex of the probe (a). The measured force as a function of time for the nanocontact test is shown in the inset of (a). Current-voltage sweeps (b) are performed during the loading and unloading of a platinum nanocontact. The slope of the linear I-V sweep is used to measure conductance G. Figure reproduced with permission from Ref. [105].

3.3 Measurement of the Contact Size from *In situ* TEM Tests[4]

The contact size in the experiments was measured using the *in situ* TEM videos. The contact diameter *2a* was measured directly from the experiments, as shown in Fig. 3a. Because of vibration in the contact and Fresnel fringes [102] around the larger-diamond indenter, the resolution of the in-contact videos are lower than the out-of-contact images. Thus, it was necessary to correct the measured contact diameter. The vibration of the indenter while in contact caused a slight broadening of the visualized contact area above the true value that would be measured if the contact were perfectly stationary. To account for this, the out-of-contact (non-vibrating) AFM probe was traced (Fig. 3b) and its shape compared to the in-contact (vibrating) shape of the same probe (Fig. 3c). The difference in the measured width of the out-of-contact and in-contact profiles was attributed to vibration-induced blurring, as shown in Fig. 3d. The mean value of the difference in the measured width was subtracted from the apparent contact diameter to determine the true contact size. The raw and corrected contact radii are shown in Fig. 3e.

[4] Much of this section appears in print: Adapted with permission from Vishnubhotla, S.B., Chen, R., Khanal, S.R., Martini, A., Jacobs, T.D.B.: Understanding contact between platinum nanocontacts at low loads: The effect of reversible plasticity. Nanotechnology. 30, 035704 (2019). Copyright © 2018 IOP Publishing Ltd.

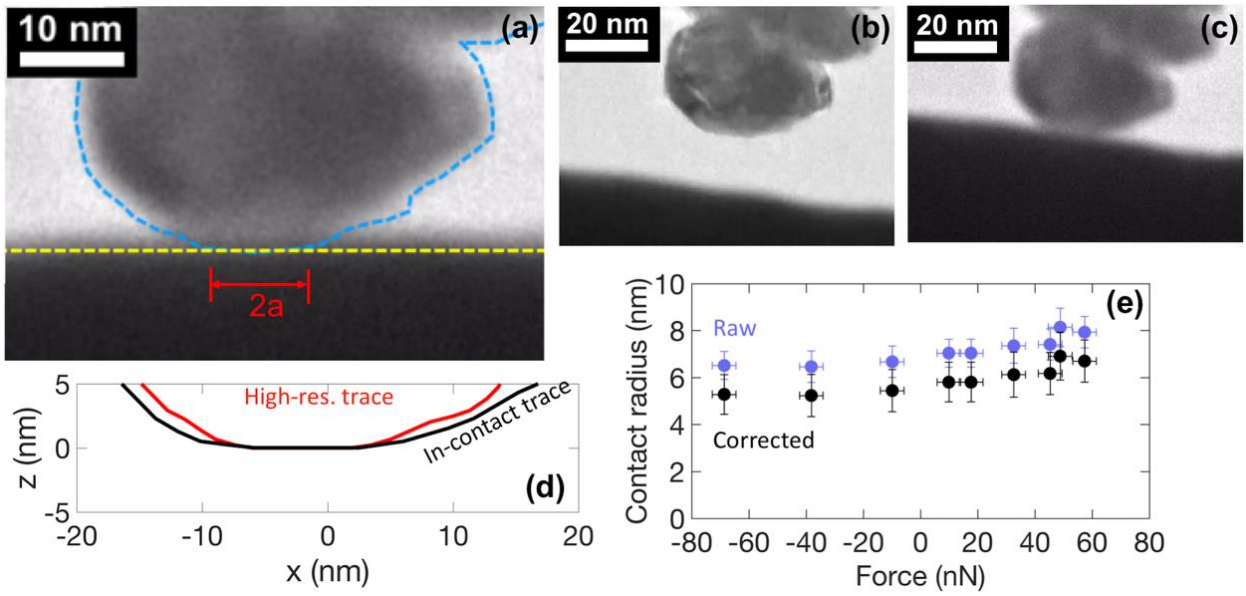

Figure 3. The contact size was determined from the frames of the TEM video (a). To account for vibration of the mechanical tester, the out-of-contact profile of the probe (b) was compared to the in-contact profile (c). The average difference between the profiles (d) was used as a measure of the vibration-induced broadening of the apparent contact size, and was subtracted from the raw value to obtain the true value (e). Figure reproduced with permission from Ref. [106].

3.4 Matched Molecular Dynamics Simulations[5,6]

Molecular dynamics simulations were used to model nanoscale contacts of the same materials system as the experiments. The atomistic model of the platinum nanocontact is shown in the Fig. 4. The high-resolution TEM image (Fig. 4a) was used to trace [107] 2D shape profile and also to measure the crystallographic orientation of the platinum. The method of disks [108] was used to create 3D surfaces for the probe shape, under the assumption that the 2D profile is representative of the probe shape in all orientations. This assumption is supported by previous work on sliding wear of silicon. For example, Ref. [109] compared side-view TEM images to the results of numerical 3D probe reconstruction from AFM scans; the results showed similar radii in all orientations. Further, using calculations for bodies of dissimilar parabolic radii in different directions [110], it can be shown that even a difference of 5% in probe radii between in-plane and out-of-plane orientations causes an error of less than 1% in computed results.

Three-dimensional model of the probes was created with matching crystallographic orientation (Fig. 4b). The height of the model probe was 9 nm. The probe size was big enough to minimize the effect of the finite system size on the contact stress distribution based on the criteria described in Ref. [111]. The model probe (Fig. 4b) was moved downward into contact with the substrate, held at the maximum load, and then pulled away from the substrate to simulate the

---

[5] Molecular dynamics simulations were conducted by Rimei Chen (PhD Candidate) in the research group of Prof. Ashlie Martini, Department of Mechanical Engineering, University of California Merced, CA, USA.

[6] Much of this section appears in print: Adapted with permission from Vishnubhotla, S.B., Chen, R., Khanal, S.R., Martini, A., Jacobs, T.D.B.: Understanding contact between platinum nanocontacts at low loads: The effect of reversible plasticity. Nanotechnology. 30, 035704 (2019). Copyright © 2018 IOP Publishing Ltd.

loading and adhesion experiments. The net vertical force on the tip atoms was calculated throughout the simulation (Fig. 4c). The number of contacting atoms was determined at intervals during the loading and unloading process and the average contact radius (Fig. 4d) was then computed from the distance between the outermost contact atoms as viewed from six different orientations (Fig. 4e).

Simulations were carried out using the molecular dynamics simulation package LAMMPS [112]. The embedded-atom method (EAM) potential was applied to model the interaction of atoms within the probe and the substrate [113]. A Lennard-Jones (L-J) potential was used to model interactions between the probe and substrate in order to reproduce the interfacial interaction strength in experiments, which could be affected by factors that are not explicitly captured in the model (e.g., surface adsorbates). Except for the time scale, the experiments and simulations are matched in terms of applied and adhesive forces, geometry, crystal orientation, and loading direction.

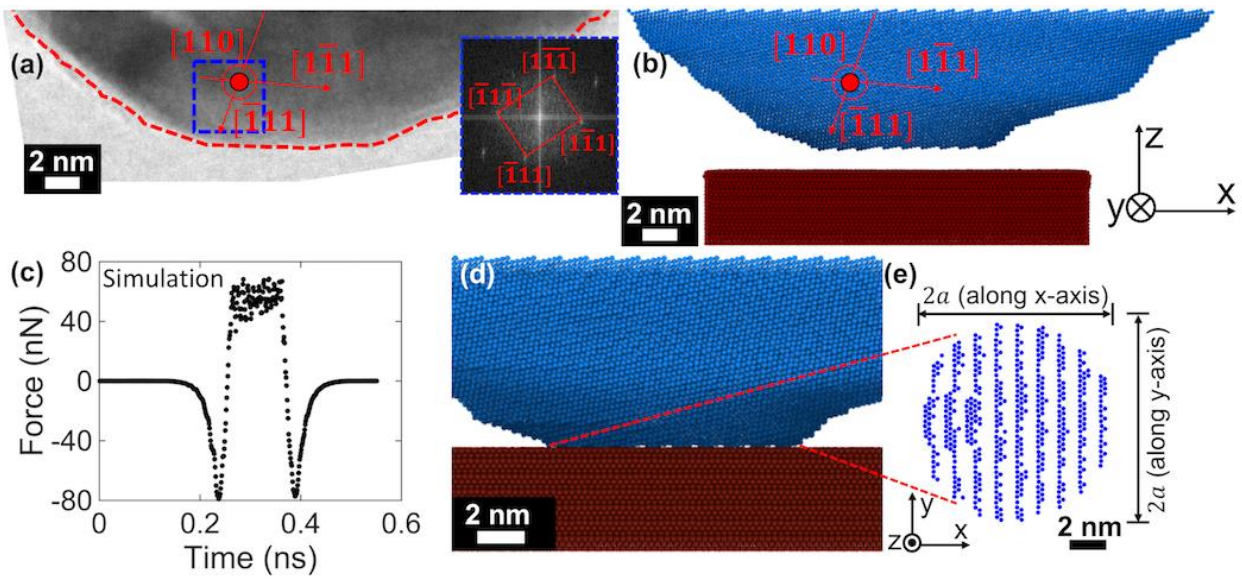

Figure 4. Matched molecular dynamics simulations were performed for *in situ* TEM contact tests. Using before-contact TEM images (a), the outer contour of the nanoscale probe was traced (red dashed line). The crystallographic orientation of the near-contact region was determined using a Fourier transform (inset) of the observed lattice planes. The geometry and crystallographic orientation were used to create an atomistic model of the probe (b) for contact simulations. The maximum and adhesive forces (c) in the experiment were reproduced in the simulations (d) and the contact diameter was measured using a top-down view of the contact (e) to facilitate direct comparison against the experimental tests. The probe (blue) and substrate (burgundy) atoms are both platinum, but are colored differently in (b) and (d) for clarity. Figure reproduced with permission from from Ref. [106].

4.0 The Effect of Dislocation Behavior on Contact Properties for Nanoscale Noble-Metal Contacts[7]

4.1 The Load-Dependence of Contact Size and Comparison against Contact Mechanics Models

The contact size as a function of applied force was measured for platinum nanocontacts using *in situ* TEM and matched molecular dynamics simulations. Five tests were performed on two separate platinum coated-AFM probes (Probe 1 and Probe 2) against a platinum substrate, in which the contacts were loaded to maximum forces ranging from 57 nN down to 0 nN (*i.e.*, under the action of adhesion only), and then unloaded to the point of separation. Matched molecular dynamics simulations were conducted for both the AFM probes using the methods described in Sect. 3.4. The interaction strength (ε) of the Lennard-Jones potential was tuned for each probe so that the simulation and experiment had the same pull-off force (Probe 1: ε_1=0.0265 eV, Probe 2: ε_2=0.0495 eV). The zero potential energy distance (σ) was taken from Ref. [114] where σ=0.241 nm for both models. The maximum force in the experiment was used to determine the maximum force for the simulation.

The load-dependent contact radii, measured with experiments and simulations, are shown in Fig. 5. The two differently-shaped probes had distinct contact areas, yet repeated tests on the

[7] Much of this chapter appears in print: Adapted with permission from Vishnubhotla, S.B., Chen, R., Khanal, S.R., Martini, A., Jacobs, T.D.B.: Understanding contact between platinum nanocontacts at low loads: The effect of reversible plasticity. Nanotechnology. 30, 035704 (2019). Copyright © 2018 IOP Publishing Ltd.

same probe showed consistent results within the uncertainty of the measurements. Further, the contact radii measured from simulations agreed with the experimental data within the uncertainty for both probes.

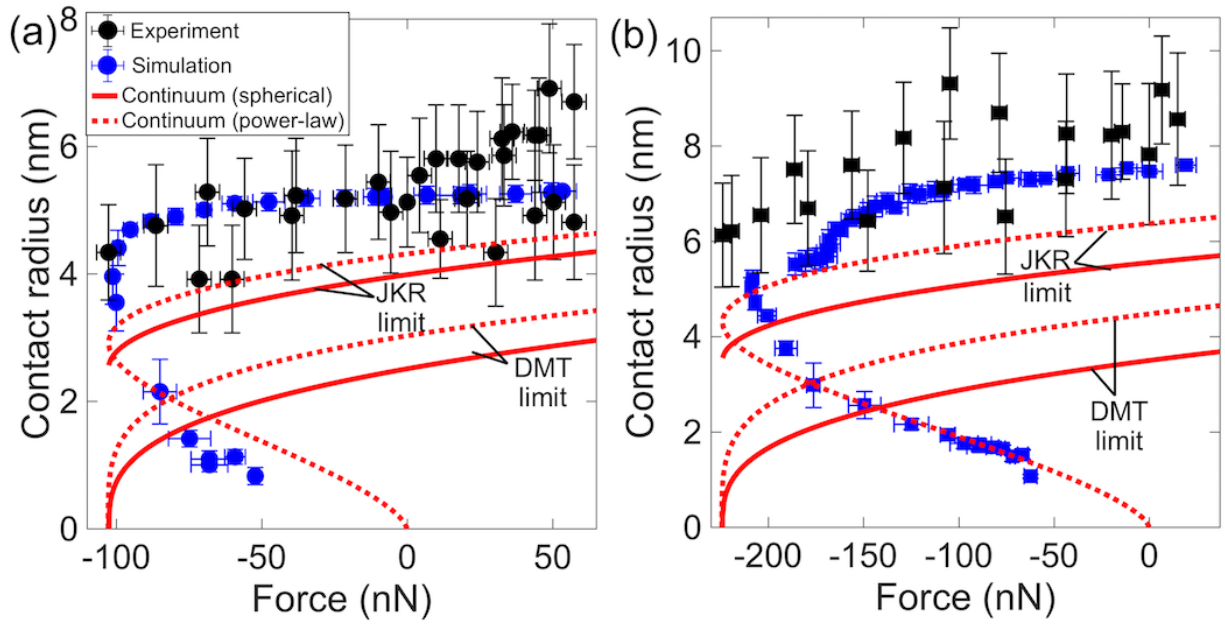

Figure 5. The contact radius is measured directly for two different nanoprobes (Probe 1 (a) and Probe 2 (b)) using *in situ* TEM tests (black symbols) as well as matched atomistic simulations (blue symbols). Multiple experimental tests and simulations of each probe agree within experimental uncertainty. These are compared with continuum predictions based on both spherical shapes (solid lines) and power-law geometries (dashed lines). With experimentally determined probe shapes and literature values for the effective modulus of platinum (100 GPa), the measured values significantly exceed the continuum predictions, by an average of 24% for the closest model and an average of 164% for the worst. Figure reproduced with permission from Ref. [106].

First, the Tabor parameter μ_T is calculated to determine which contact model can be applied to platinum nanocontacts. The Tabor parameters for the two AFM probes were calculated using best-fit sphere radii of 20.5 nm and 25.4 nm (Fig. 6b,e), respectively, and measured pull-off forces

of 103 nN and 224 nN, respectively. The effective modulus E^* = 100 GPa was computed using the elastic modulus E = 169 GPa and the Poisson ratio ν = 0.39 of platinum [115], and z_0 was assumed to be in the range 0.2 – 0.3 nm [22]. The resulting values were μ_T = 0.4 – 1.0, which indicate that the contacts are nearer to the DMT limit of behavior.

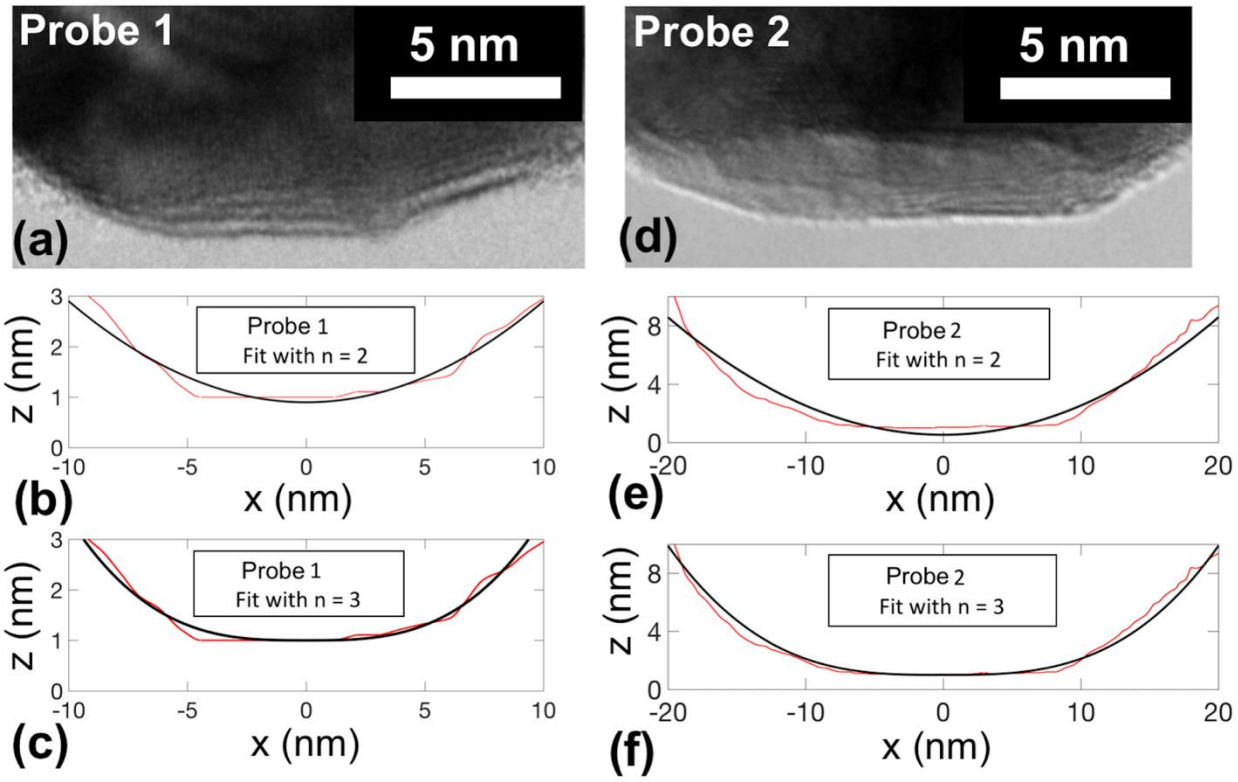

Figure 6. The extracted shapes of the probes (red) from the TEM images (a, d) fit using power law function with power index n = 3 fit best in comparison to spherical shape (n =2) for the probe 1 (b, c) and probe 2 (e, f). For n = 2, the best-fit radii were R = 20.5 nm and 25.4 nm for probe 1 and 2, respectively. For n = 3, the best-fit curvature of the profile was Q = 137 nm^2 and Q = 300 nm^2 for probe 1 and 2, respectively. Figure reproduced with permission from Ref. [106].

Second, the load-dependent radii measurements were compared against the predictions of common spherical adhesive contact models: JKR and DMT. These predictions are calculated using the Eq. 2-4 and Eq. 2-6 for DMT and JKR respectively and are shown in Fig. 5. The contact size measured in experiment and simulation was larger than the predicted values from the contact mechanics models by an average of 164% for DMT and 40% for JKR. For contacts in the intermediate regime (as described by the Maugis-Dugdale model), the predictions will lie in between these limits. Third, the data was compared to predictions from the non-spherical power-law models. The power-law function ($z(r) = r^n/nQ$) was fit to the probe shape obtained from the TEM images of the two platinum probes (Figs. 6c,f). The fit was performed using the linear least squares method for values of *n* from 2 to 10. The best-fit power index was determined to be $n = 3$ with $Q = 137$ nm^2 and $Q = 300$ nm^2 for Probes 1 and 2 respectively, indicating that the power-law model was expected to describe the data more accurately than one assuming a spherical (or parabolic) shape (Fig. 6). The power-law contact model predictions calculated using the Eqs. 2-11(a-d) with n = 3 for DMT and JKR limits is shown in Fig. 5. The JKR-n model is the closest of the four models, but the predictions still deviate by an average of 24% from the measured data. For the spherical and power-law models, the JKR-limit of behavior was significantly closer to the measured results than the DMT behavior, despite the fact that the Tabor parameter indicates that the behavior should be closer to that of the DMT model.

The load-dependent contact size can be accurately fit using the power-law continuum model *only* if the effective modulus is treated as a free parameter. In this way, the behavior of both probes is accurately fit using the JKR-limit of behavior for a power-law shaped probe (JKR-n) as shown in Fig. 7. Specifically, best-fits to Probes 1 and 2 yield values for the effective modulus of $E^* = 41$ GPa and $E^* = 44$ GPa respectively – more than a 50% reduction below the value for

platinum. This fitting is *not* meant to imply that the local elastic modulus of the material is actually reduced below the true value for platinum. Instead, the apparent reduction in modulus is an empirically-derived correction to contact mechanics, which quantifies the apparent softening of the platinum nanocontacts. The physical origin of this softening is discussed in the next section.

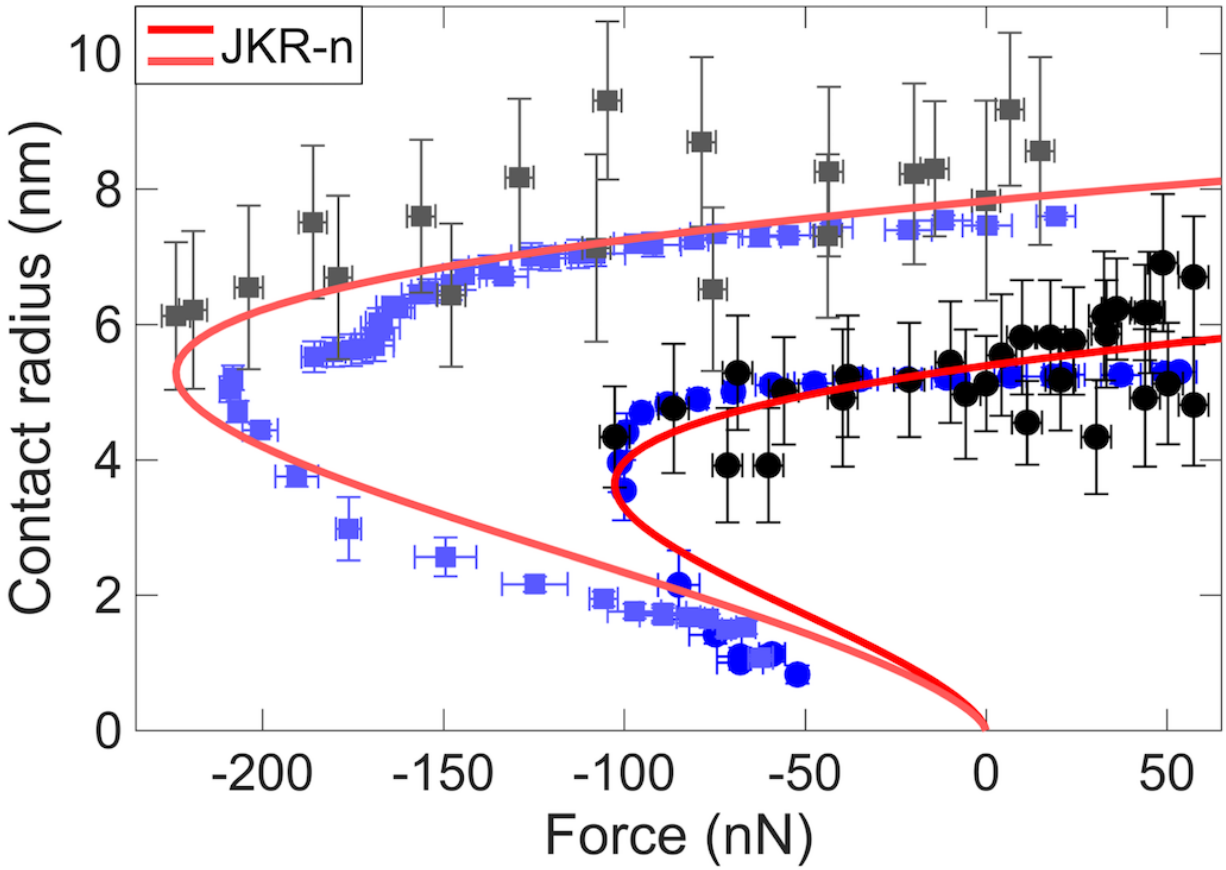

Figure 7. The true contact size can be accurately fit with mechanics models only if the effective modulus is used as a free parameter. The measured contact radius vs. force data is shown for Probe 1 (bottom data, darker color) and for Probe 2 (top data, lighter color). The experimental (black) and simulation (blue data) are best fit using a power-law-shaped continuum model in the JKR-limit (red lines) with an effective modulus of 41 and 44 GPa for Probes 1 and 2, respectively. This empirically measured effective modulus is less than half of the true value for platinum. Figure reproduced with permission from Ref. [106].

4.2 The Role of Dislocation Activity in Increasing Contact Size

One possible explanation for the larger-than-expected contact size is plasticity-induced permanent shape change in the bodies, as is common in traditional high-load nanoindentation [116]. Therefore, the post-test probes were examined for evidence of shape change and/or crystal defects. For both the experimental and simulated probes, the shapes were measured by digitally tracing [107] the outermost contour of the probes using side-view images (as shown in Fig. 4a). In all cases, when the pre-test and post-test shapes were compared, the geometries remained virtually identical (Fig. 8a,b). The experimental probes did not show detectable variation (Fig. 8a) within the accuracy of the edge-detection technique; the simulated probes exhibited minimal shape change as well (Fig. 8b). High-resolution examination of the experimental probes after contact (Fig. 8c,d) showed no evidence of significant crystal defects, with near-perfect lattice up to the surface of the probe apex. The post-test simulation probes were analyzed using a local lattice analysis, and showed no evidence of dislocations or other lattice defects. Furthermore, the contact size was non-hysteretic upon loading and unloading, and behaved consistently when repeated multiple times in experiment and in simulation. Therefore, the origin of deviations in contact area from continuum models could not be explained by plasticity-induced permanent shape change.

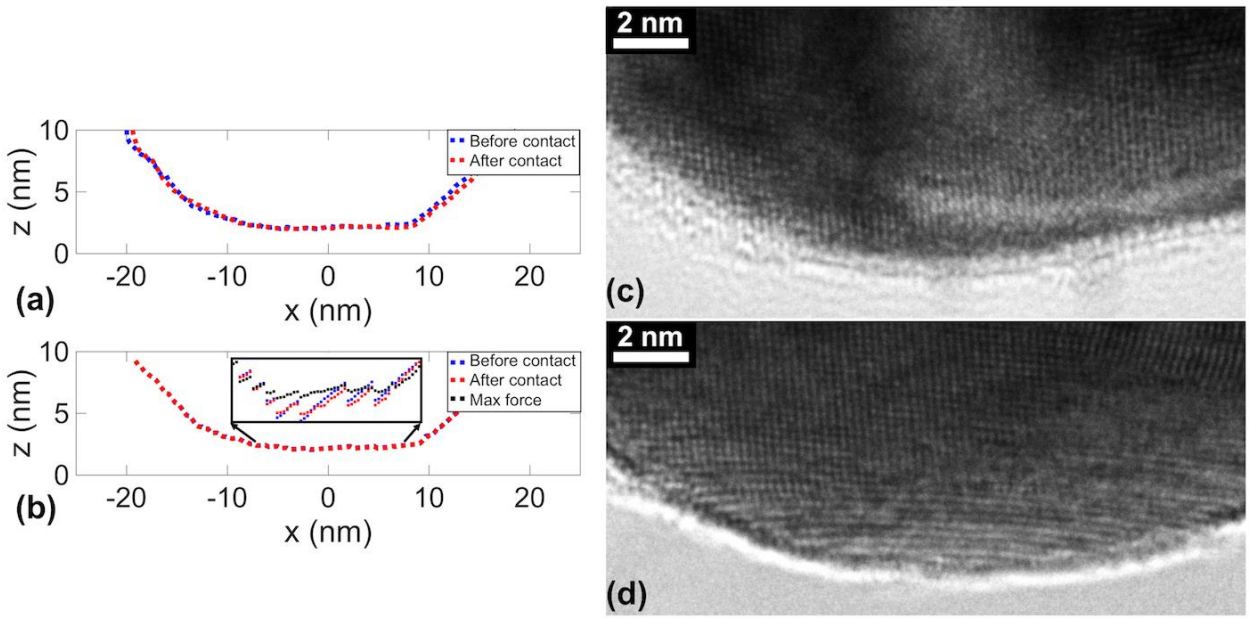

Figure 8. In comparing the profiles of the probe in TEM before and after contact (as shown in (a)), no shape change was observed within the accuracy of the edge detection in any tests. Similarly, the probe shape in simulations was nearly identical before and after contact (b). The inset to (b) shows the central region of the probe with a highly scaled-up z-axis (16 nm in width, 0.5 nm in height). The surface steps that are present before contact are smoothed out at the maximum force of 14 nN, but then are restored upon unloading. High resolution imaging of Probe 1 before (c) and after (d) the test showed no evidence of dislocations within the atomic lattice up to the surface of the probe. Figure reproduced with permission from Ref. [106].

Next, reversible dislocation activity was assessed. The simulated probes were examined during loading and unloading by visualizing non-equilibrium atoms, as shown in Fig. 9. The platinum probe started out dislocation-free and remained that way on initial adhesive approach. Then, upon further loading, Shockley partial dislocations (b = 1/6<112>) nucleated at surface step edges (which are apparent in the inset to Fig. 8b) and propagated into the crystal. The number and length of dislocations increased up to the maximum applied load, at which point there were 26 dislocations, for a total line length of 42.8 nm (Fig. 9b). Upon unloading, the dislocations were

driven back toward the surface. The number and length of dislocations decreased monotonically upon unloading, with the probe left in a defect-free state by the end of the test.

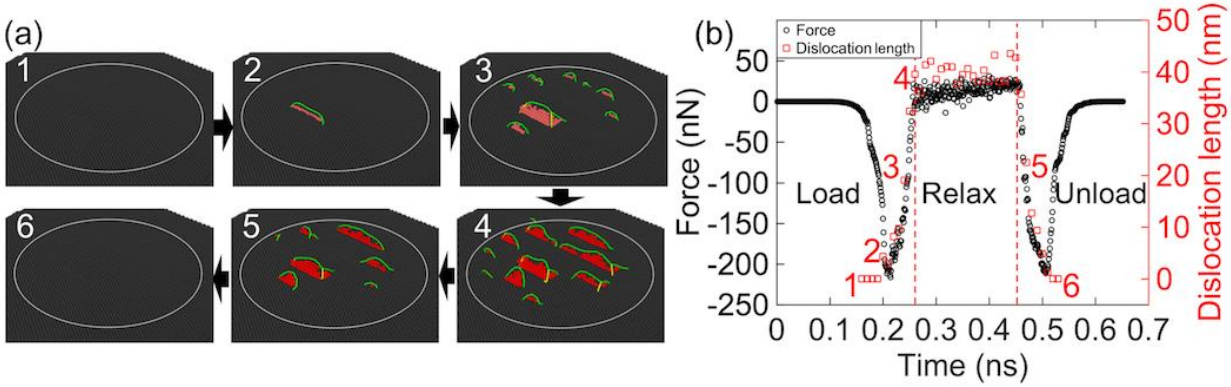

Figure 9. The simulations revealed significant dislocation activity, which began at the lowest applied loads and was fully reversed upon unloading. The platinum probe is shown in (a) at various loads (corresponding to the numbered points identified in panel (b)). Non-defected FCC atoms in the probe have been removed for visibility. The green and yellow lines represent Shockley and Hirth partial dislocations, respectively, and locally HCP atoms are shown in red. The substrate is shown in black, and remained dislocation-free throughout testing. The probe was dislocation-free before testing. Upon loading, partial dislocations nucleated at surface steps and migrated a load-dependent distance into the material. Upon unloading, the dislocations moved back to the surface, restoring the step edges, and leaving the probe dislocation-free after testing. Figure reproduced with permission from Ref. [106].

Using the DMT model as an approximate guide, the compressive pressure decays rapidly with depth, decreasing by 50% between the surface and a depth equal to the contact radius. This limits the depth to which dislocations can propagate. Upon unloading, the local stress is reduced, and eventually the contact becomes purely adhesive. Because of this adhesion and also the well-known image force [117] that dislocations feel from nearby surfaces and interfaces, the dislocations are driven back towards the surface during unloading. They eventually exit the

material, restoring the surface steps and the original shape of the probe (as shown in the inset of the Fig. 8b). This dislocation activity results in significantly enhanced contact area compared to purely elastic predictions, but without the bulk shape change that would be predicted by plasticity models (such as Refs. [118, 119]).

This investigation differs from prior experimental investigations because it explores the behavior of nanoscale contacts under ultra-low loads, in the regime where continuum contact mechanics models are often applied and expected to have validity. The significant effect of fully-reversed dislocation activity that is seen here is not typically observed in uniaxial tension or compression of nanowhiskers or nanopillars [120]. In those cases, the stress is approximately uniform throughout the material, and the applied loads are typically larger than the adhesive loads. Thus, dislocations can propagate through the material, exiting the other side and leaving behind irreversible plastic strain. Fully-reversed dislocation activity *has* been observed [69] in cryogenic nanoindentation to higher loads on gold, but these effects had not yet been measured in other materials, nor in applications-relevant conditions: namely room temperature and low (adhesion-dominated) loads. Further, the effect of reversible plasticity on contact size had not been explored previously.

This investigation also differs from prior simulation and numerical investigations that examine the applicability of continuum contact mechanics because most of those focus on the effect of atomic corrugation on contact properties. One such avenue of investigation [43, 44] discussed explicitly how a body with nanoscale curvature cannot have a truly continuum-like shape, but rather must be composed of discrete surface steps. In that fully-elastic simulation, it was shown that these surface steps led to stress concentrations at the edges (similar to those of a Boussinesq punch [121]). They also led to discrete jumps in the number of contact atoms as a

function of load, as each new layer was pressed into contact. The present investigation extends this understanding further; the surface steps serve two critical roles that were not discussed in that prior work: (1) dislocation nucleation at surface steps; and (2) and the flattening of contact caused by those dislocations, each discussed in the next paragraph.

First, the surface steps act as easy nucleation sites for dislocations, as evidenced in the present simulations by the fact that dislocations initiate at points where surface steps come into contact with the substrate (Fig. 9a). In nanoindentation to larger loads, surface steps on flat surfaces have been shown to act as dislocation nucleation sites [122–124]. The effect is magnified in nanocontacts where one or both of the bodies has nanoscale curvature; the surfaces are prevalent and surface defects (which are necessary to accommodate the curvature) provide ample locations for dislocation initiation. The second aspect that was not considered in the prior work on nanoscale contact area [43, 44] is the flattening of the surface. The crystal slip that is associated with these surface-step-nucleated dislocations allows these most-prominent surface features to recede by one burgers vector, thus locally flattening the original topography of the probe (inset to Fig. 8b). This reversible crystal slip serves to increase the contact area above the fully elastic predictions for a stepped surface. Finally, because surface steps like these are common for crystalline bodies with nanoscale curvature, the observed effects of reversible dislocation plasticity and larger-than-expected contact sizes are predicted to be a very common feature in contacts between metallic nanostructures.

4.3 Conclusions Regarding the Accuracy of Contact Mechanics Models for Noble-Metal Contacts

In summary, loading and adhesion tests were performed on platinum nanoprobes under controlled load inside of a transmission electron microscope. The contact radius was directly measured using *in situ* observation. Atomistic simulations were performed on similar platinum nanoprobes with matched geometry, crystallographic orientation, loading direction, and applied and adhesive loads. The experimental and simulation measurements of load-dependent contact size agreed within experimental uncertainty, but exceeded the predictions of spherical continuum contact mechanics by 40-164%. The agreement with continuum predictions was improved by using a non-spherical power-law-shaped model, but the best fit still deviated by 24% when using literature values for material properties. As an empirical correction to contact mechanics, the load-dependent contact size could be accurately fit using a dislocation-mediated apparent effective modulus of 43 ± 2 GPa instead of the true value for platinum of 100 GPa. The physical mechanism for this increase in contact area was shown to be dislocations nucleating at surface steps and propagating a short distance into the material. The dislocation activity was fully reversed upon unloading, leaving the experimental and simulation probes free of dislocations, even after repeated testing. These findings have implications for probe-based microscopy and lithography, and for nanostructures in device applications, where continuum mechanics is often used to predict behavior.

5.0 The Relationship Between the Contact Size and Conductance for Nanoscale Noble-Metal Contacts[8]

5.1 Comparing the Measurements of Contact Radius with Electron Transport Predictions

The direct measurements of the contact radius is compared against the values computed using electrical transport measurements. Five adhesion and loading tests were performed with real-time evaluation of contact radius and current flow for platinum nanocontacts. Figure 10 shows a comparison of the directly-measured contact radius obtained from TEM and atomistic simulations against the computed contact radius obtained from applying electron transport theories to the measured current flow. The five individual tests showed consistent results within the uncertainty of the measurements (Fig. 10a,b) and the simulation-determined contact radius matched well with the contact radius obtained from the experiments. Here, the contact size was computed from experimentally-measured conductance using both limits (ballistic and diffusive), with well-established properties of platinum: bulk conductivity $\sigma_{bulk} = 94.3 \times 10^{-3}$ $(\mu\Omega\ \text{cm})^{-1}$ [75, 125–127]; and mean free path length $l_f = 7$ nm, calculated using the free-electron model [126]. The results show that the contact radius calculated from the current flow using ballistic and diffusive electron transport theories is, on average, 95% smaller than the direct measurements. This suggests that

[8] Much of this chapter appears in print: Adapted with permission from Vishnubhotla, S.B., Chen, R., Khanal, S.R., Li, J., Stach, E.A., Martini, A., Jacobs, T.D.B.: Quantitative measurement of contact area and electron transport across platinum nanocontacts for scanning probe microscopy and electrical nanodevices. Nanotechnology. 30, 45705 (2019).

these transport theories do not accurately describe the present contact. The physical origin of this discrepancy is discussed in the next section.

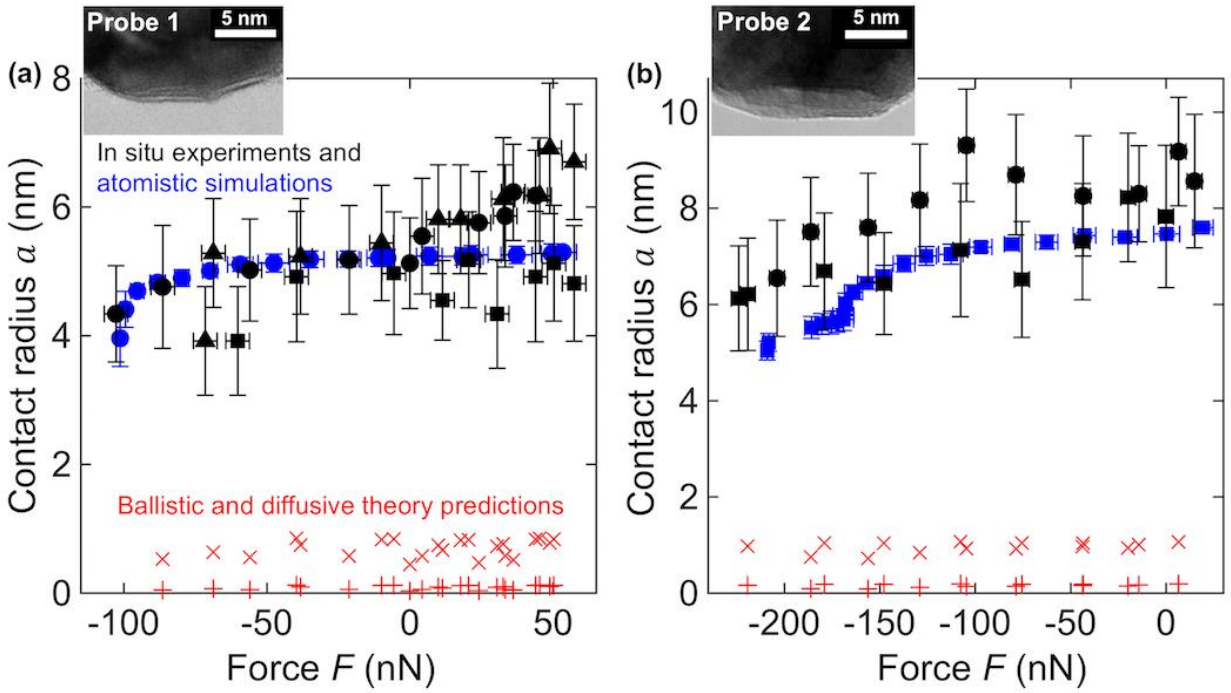

Figure 10. The directly measured contact radius varies significantly from the value computed from electrical measurements. The contact radius from *in situ* experiments (black symbols) and atomistic simulations (blue symbols) is shown as a function of applied force. Multiple repeated measurements showed consistent results for two different platinum nanoprobes (shown separately in panels (a) and (b)). The contact radii computed from the electrical measurements, using the limiting cases of diffusive (crosses) and ballistic (plus symbols) transport, were lower than the direct measurements by 95%. Figure reproduced with permission from Ref. [105].

5.2 Investigating the Physical Origin of the Low Contact Conductance

To explore the physical origin of the lower-than-expected conductance, we considered three possible hypotheses. (1) The current flow is reduced because of significant inelastic scattering of electrons at defects in the near-surface region. (2) The true atomic contact area is much smaller than the apparent contact area due to, for example, atomic-scale corrugation and surface roughness, thus significantly reducing current flow. (3) The presence of thin insulating surface species, such as oxygen or adventitious carbon, significantly reduces the metal-metal contact or eliminates it altogether, requiring electron tunneling. These are considered individually in the following paragraphs.

The basis for the defect-scattering hypothesis (Hypothesis 1) is prior work, including that of Mayadas and Shatzkes [128], which demonstrates significant scattering from defects in confined systems. While defect scattering is negligible in bulk contacts, it is a significant factor in nanograined metals which have a large density of crystal defects [129]. In the Sect. 4.2, it was shown that for the same platinum contacts, the defect density in the near-surface region is very large, even at ultra-low (adhesion-only) loads. The defect-scattering hypothesis leads to the specific prediction that the degree of electron scattering will be inversely proportional to the defect spacing in the material [128]. To test this prediction, the scattering factor was computed in the present work and compared to the defect density in the material (which is inversely proportional to the defect spacing). Instead of the ratio of ρ/ρ_{bulk} used by Mayadas and Shtazkes for large 2D films, we computed the scattering factor as the ratio of conductance predicted using the intermediate theory (G_I, computed using Eq. 2-13 with the TEM-determined contact size) divided by the measured conductance G from the experiment. As shown in Fig. 11a, while there is significant increase in dislocations with increasing force, the measured scattering factor exhibits

no consistent trend with force. Thus, the predictions of the Mayadas and Shtazkes model are not supported by the data, which suggests that scattering from defects is not the primary cause of low conductance in these contacts.

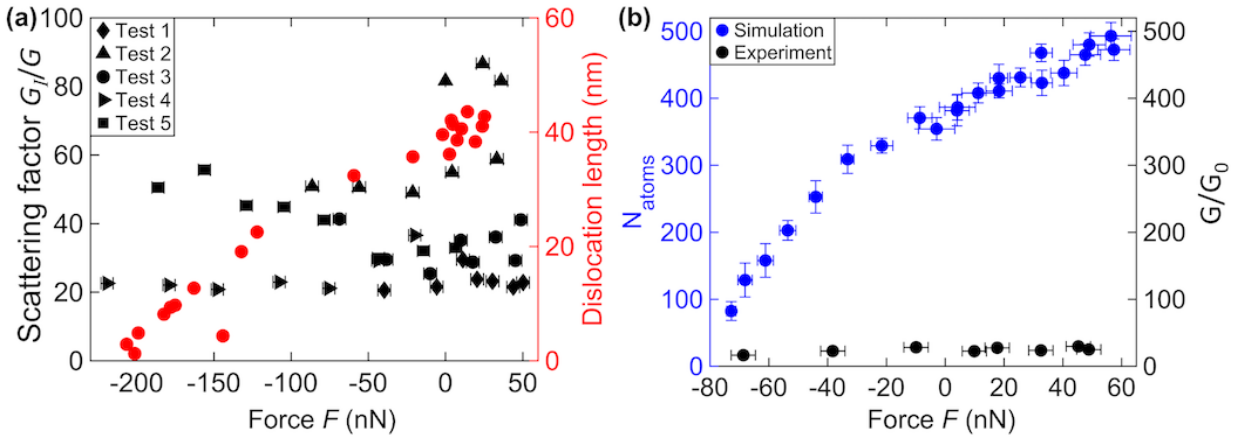

Figure 11. To evaluate the effect of electron scattering from defects, a scattering factor (a) was computed (see main text) and compared to the length of dislocations in the tip material. No correlation between these was observed, with scattering factor approximately constant with force for most tests and dislocation length increasing monotonically. Thus, the defect-scattering hypothesis is not supported. The analysis of dislocations in these contacts is described in Sect. 4.2. To evaluate the possibility of roughness-induced incomplete contact, the number of atoms in contact (b) was determined from the atomistic simulations and compared to the ratio G/G_0, which would reflect the number of contact atoms in the case of ballistic transport across a number of very small contacts. These two curve exhibits very different magnitudes and trends with force, implying that this is not the cause of the low contact conductance. Figure reproduced with permission from Ref. [105].

The hypothesis of patchy atomic contact (Hypothesis 2) is based on prior experimental investigation of the electrical and thermal transport across the nanoscale interfaces [80, 130] as well as atomistic simulations of nanoscale probes [41, 48, 80, 130–132], which have suggested

that the true atomic contact that contributes to transport may be much smaller than the overall contact area. This is commonly attributed to surface roughness, even down to atomic-scale corrugation of the surface. Roughness or corrugation can cause the contact to behave as a collection of atomic-scale point contacts, rather than a single nanoscale junction, resulting in significantly reduced transport. In the present testing, the idea of patchy contact can be tested by directly computing the number of contact atoms from the molecular dynamics simulations and comparing to the number of contact atoms calculated from the conductance. The latter quantity is computed by dividing the total measured conductance by the conductance quantum G_0 $(12.9\ k\Omega)^{-1}$ [133–138]. If the nanocontact is behaving as a small number of atomic junctions, then G/G_0 should be approximately equal to the number of atoms in contact. As shown in Fig. 11b, the number of contact atoms from the simulation is far greater (between 8 and 19 times greater) than the computed number of contact atoms determined from the electrical conductance. Further, it can be observed from Fig. 11b that at the maximum force of 57 nN, the number of atoms in contact calculated from ballistic contact is 25 in comparison to 500 in the simulations. This implies that roughness and patchy contact result in a 95% reduction in contact area. This seems extremely unlikely as it would require the remaining 5% of the contact atoms to carry twenty times more load per atom than for full contact. The contact stress was already large (9 GPa at maximum force, as calculated using contact mechanics models and assuming full contact), and a 20-fold increase above this would almost certainly lead to flattening of any local protrusions. Such flattening would reduce patchiness and result in near-complete contact. It should also be noted that any such roughness would be explicitly rubbed off in the sliding tests that are described below in Sect. 5.3; yet these tests showed no significant increase in conductance. These findings suggest that the failure of ballistic transport equations cannot be explained by surface roughness and atomic corrugation.

Finally, in the surface-species hypothesis (Hypothesis 3), the low conductance arises because of insulating species that are present on the surface, likely either oxygen or adventitious carbon from exposure to air before testing. In this case, tunneling theory [139] is expected to predict the electron transport better than ballistic or intermediate models. For an insulating layer between two similar metals, at very low voltages, Simmons *et. al.* [139] provided an expression for the current density J (in units of A/m^2) as a function of applied voltage V (in V) as:

$$\mathrm{J} = 3.16 \times 10^{14} \sqrt{\phi} \left(\frac{V}{\Delta z}\right) \exp\left[-1.025 \Delta z \sqrt{\phi}\right] \tag{5-1}$$

where ϕ is mean barrier height (in eV), Δz is barrier width (in Å) which can be assumed to be thickness of the insulating layer [139]. For fixed values of ϕ and Δz, the current density is linearly proportional to applied voltage, similar to the behavior of Ohmic contact [139]. Hence, Eq. 5-1 can be written in terms of conductance, contact area $A_{electrical}$, and tunnel resistivity $\sigma_T (= V/J)$ as follows:

$$G = \frac{A_{electrical}}{\sigma_T} \tag{5-2}$$

where the units are as follows: G in Ω^{-1}, $A_{electrical}$ in cm^2, and σ_T in Ω cm^2.

The tunneling model described by Eq. 5-2 is fit to the experimental data (Fig. 12a) with tunnel resistivity as the free parameter. The extracted best fit for σ_T is 6.7×10^{-10} Ω cm^2. The order of magnitude of the best-fit tunnel resistivity is reasonable for an insulating material having thickness less than 2 nm at very low voltages [139]. The tunnel resistivity σ_T is a function of mean

barrier width and potential barrier of the insulating material. Specifically, using the best-fit tunnel resistivity and the measured thickness of the layer, the potential barrier ϕ can be determined. High-resolution images of the probes before and after contact were used to attempt to determine the thickness Δz of the hypothesized insulating layer. As shown in Fig. 12b, the platinum appears to persist all the way to the surface, with no clear surface layer observed. Therefore, we used the resolution of the TEM (0.23 nm) as an upper-bound estimate of the thickness of the surface layer, which is consistent with earlier work using aberration-corrected environmental TEM to oxidize and reduce a platinum surface [140]. Using the best-fit tunnel resistivity (6.7×10^{-10} Ω cm^2) with a layer thickness of 0.23 nm, the barrier height computed using Eq. 5-1 is 0.8 eV (Fig. 12c). The electrical contact area predicted using Eq. 5-2 is consistent with direct measurements of experiments and simulations (Fig. 12d).

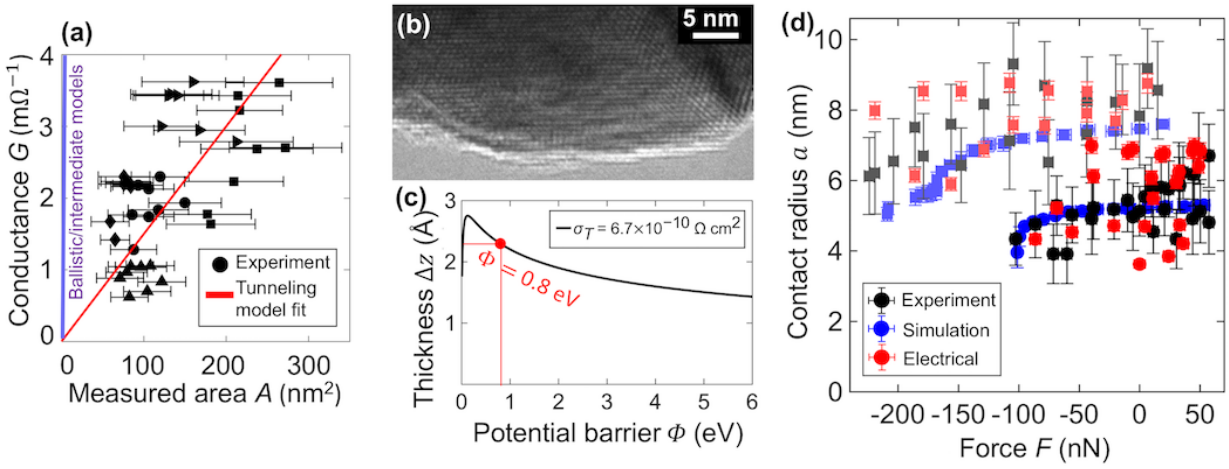

Figure 12. The conductance across the platinum nanocontact (a) is proportional to the experimentally observed contact area, within experimental uncertainty, but is not consistent with ballistic and intermediate theories. Under the assumption of electron tunneling, the proportionality constant yields a measure of the tunnel resistivity. Since surface species cannot be observed in high-resolution TEM (b), the imaging resolution (0.23 nm) is taken as an upper-bound of the insulating film thickness. These data can be combined with tunneling theory (c) to measure a potential barrier for the surface layer of $\boldsymbol{\phi}$ = 0.8 eV. Using tunneling-mediated transport with the best-fit parameters, the electrical measurements can be used to extract a contact size (shown in d) that is consistent with experiments and simulations. Figure reproduced with permission from Ref. [105].

5.3 Investigating the Robustness of the Low Contact Conductance

To investigate the consistency and robustness of the low contact conductance, 14 more tests were conducted on a new platinum coated AFM probe. In these tests, the current density was repeatedly measured with periodic intervals of lateral sliding. The sliding was performed under applied forces of 0−30 nN with periodic current-voltage sweeps to monitor conductance, all under high vacuum (p = 10^{-5} Pa). The probe was slid for a total sliding distance of 1200 nm, which led

to the removal of approximately 3.4 nm of probe height due to sliding wear, as shown in Fig. 13a-c. The current density throughout the 14 tests was computed as the measured electrical current (at the bias of 0.01 mV) divided by experimentally measured contact size, and is shown in Fig. 13d. While there is random fluctuation in the data, the current density remained approximately constant at 15 kA/cm^2 throughout all tests. The current density never approaches the value expected for a pure-platinum ballistic contact, which is approximately 600-1000 kA/cm^2.

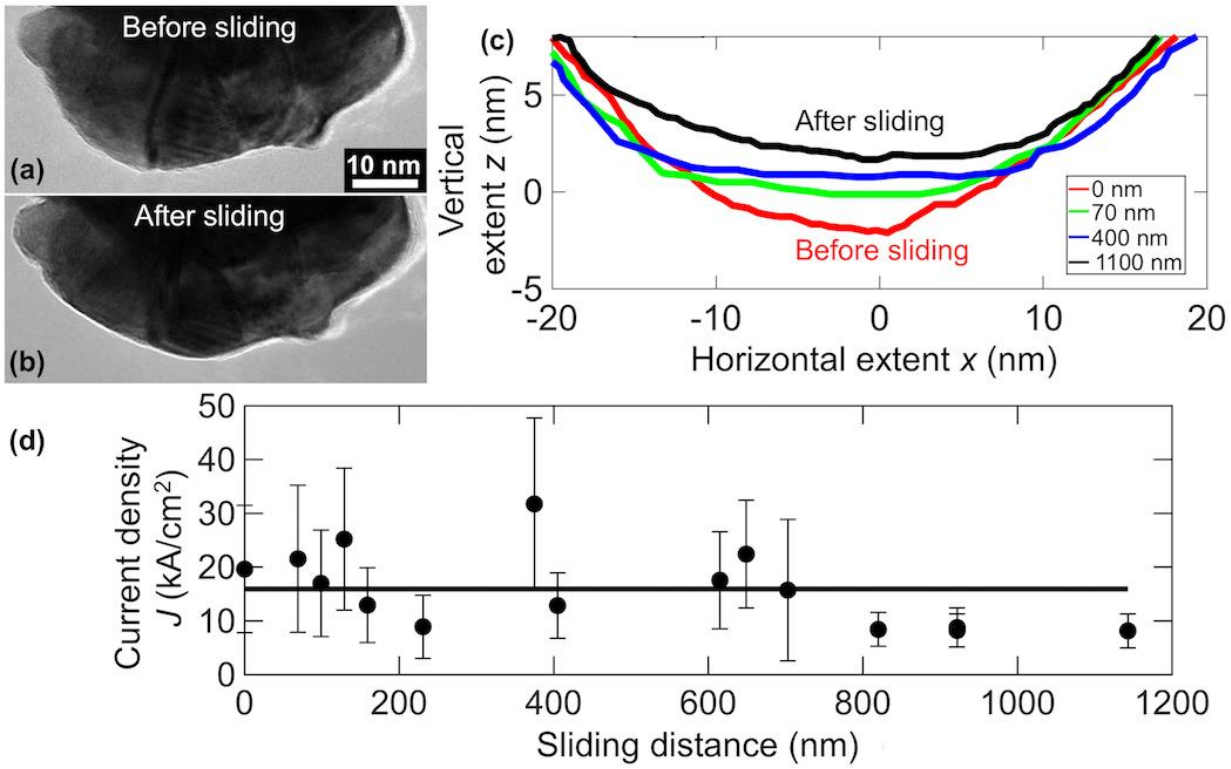

Figure 13. A platinum probe was slid laterally with periodic current-voltage sweeps. The images of the tip before (a) and after (b) sliding show clear evidence of tip wear, with significant shape change and more than 3 nm of loss of tip height (c). However, the current density remained at an average of 15 kA/cm^2 throughout the testing (d). This indicates that the low contact conductance is robust, even with changes in probe shape. Figure reproduced with permission from Ref. [105].

The purpose of these sliding tests was not only to mimic the sliding of an AFM probe, but also to cause sliding wear of the probe apex. This sliding wear served two purposes: disruption of surface layers; and modification of probe shape. First, the low conductivity persisted despite the disruption or removal of the surface material. This finding indicates that even as surface species are removed, they are rapidly redeposited, either from surface species on the substrate or from residual species in high-vacuum TEM chamber. Second, the current density was consistent despite significant changes in probe shape. This finding indicates that the low conductance is not an attribute of the particular shape of these chosen probes, but rather is generalizable to a wide variety of probe shapes. Because of the time-intensive nature of *in situ* TEM electromechanical tests, it is impractical to test a large number of distinct AFM probes. Instead, by modifying the shape of the probe through sliding wear, this set of tests enabled the investigation of current density for 14 different shapes of the probe tip. The testing described in Sect. 5.2 established that the low current density was robust to loading; the testing in this section demonstrated the consistency despite sliding and changes in probe shape. Overall, the lower-than-expected contact conductance is shown to be a persistent feature of platinum nanoprobes, and is therefore also likely to be present in technologically relevant platinum nanocontacts.

5.4 Implications of Robust Insulating Layer to SPM and Nanodevices

While it is well known that small amounts of oxide or contamination can affect contact conductance, this investigation demonstrates the significant and persistent role that surface layers play in nanoscale contacts composed of platinum. Even when tested in vacuum, and with the contact subjected to sliding wear, the conductance remains significantly lower than what is

predicted by electrical transport theory. The persistence of this surface layer may arise due to tribochemical processes that occur on platinum contacts [98]. It has been shown using DFT that the polymerization reactions could take place with a threshold stress of 24 GPa on a flat platinum surface and this threshold stress can be even lower due to shear stresses as well as surface steps and vacancies [98]. In the present investigation, the maximum contact stress reached during loading is more than 9 GPa (This is the value computed using contact mechanics models applied to the overall tip shape [19], but local asperities will lead to stress concentrations above this value). Also, the simulations provide evidence for surface steps which can be observed on the model AFM probe (Fig. 4b,d). Hence, these tribochemical processes could explain the presence and robustness of the insulating monolayer.

The present findings of low contact conductance shed some light on the widely observed [28, 80, 96, 141] phenomena of higher-than-expected contact resistance in conductive AFM. For instance, Celano and co-workers [80] introduced a precise calibration procedure to determine the electrical contact area of an AFM probe. Current-voltage sweeps were performed on a silicon oxide substrate of precisely 1.5 nm thickness; then, using tunneling theory to describe the conductance through the oxide, the size of the current collector (*i.e.*, the contact) could be determined. From measured current flow through a Pt-Ir probe, a contact radius of just 0.69 nm was computed at a load of 78 nN and 0.97 nm at 157 nN. The authors commented on this being far smaller than the expected size from contact mechanics with an assumed probe radius of 30 nm. The authors do not suggest an explanation for this ultra-small electrical contact size, except potentially microroughness (yet TEM images [96] of similar probes from the same manufacturer do not demonstrate such extreme roughness). The present results rule out this type of roughness as the origin of the low current, as well as defects in the near-surface material, and instead suggest an

explanation for the ultra-small measured contact size. The nanoscale metallic probe itself is suggested to have lower-than-expected conductance, due to surface species which are not accounted for in Celano's investigation. If we apply an empirical correction (Eq. 5-2) to this calculation, where the contact conductance is 95% smaller than predicted by ballistic transport theory, then the computed contact area rises from 1.5 nm^2 to a value of 30 nm^2, which is consistent with the authors' prediction of 28 nm^2 for a 78 nN load.

5.5 Conclusions Regarding the Relationship between the Contact size and Conductance for Nanoscale Noble-Metal Contacts

In summary, the contact radius was directly measured using *in situ* observation, and the contact conductance was measured using real-time current-voltage sweeps. The application of electrical transport theories to the measured conductance yielded measurements of contact size that were 95% smaller than the experimental and simulation values. Two possible explanations for the lower-than-expected contact conductance were ruled out: electron scattering from crystal defects; and a roughness-induced reduction in contact area. Instead, the physical mechanism for this deviation from electron transport theories was found to be the presence of insulating surface species. The observed reduction in contact conductance was consistent despite loading and sliding of the probe, and was maintained even as the probe shape was modified due to sliding wear. Tunneling theory was empirically fit to the data, based on approximately monolayer coverage (roughly 0.23 nm) of insulating species with a measured potential barrier of 0.8 eV. It is suggested that this description, tunneling theory with these best-fit parameters, provides a more robust method than ballistic electron transport for the calculation of contact area for single-asperity

platinum contacts from the current-voltage data in AFM, and for the prediction of current in platinum nanodevices.

6.0 The Effect of the Applied Pressure on the Adhesion Strength of Covalently Bonded Material Contacts

6.1 *In situ* TEM and Matched Simulation of Silicon Diamond Nanocontact: Insights from Single Contact Test[9]

6.1.1 Molecular Dynamic Simulation of Matched Silicon Diamond Nanocontact

Experimental contact test was performed between a silicon AFM probe and a flat diamond substrate (see Sect. 3.1 and Fig. 1). The atomistic model of the silicon probe (Fig. 14b,c) is created using the outer profile shape and crystal orientation from the high-resolution TEM image (Fig. 14a and see Sect 3.4). The height of the probe model was 10 nm. The substrate consisted of carbon atoms in a diamond lattice and had dimensions of 20 × 20 × 1 nm in the *x, y,* and *z* directions respectively. The substrate atoms were held rigid for computational efficiency. According to the Hertz model, this assumption is expected to introduce differences in contact area and deformation of approximately 7% from the experiment. However, this was accepted since an accurate description of elasticity on both bodies would have required a significant increase in the simulation size. The substrate was modeled as a flat surface because the radius of curvature of the overall shape of the diamond indenter was measured to be 1 μm. Nanoscale roughness on the substrate

[9] Much of this section appears in print: Adapted with permission from Vishnubhotla, S.B., Chen, R., Khanal, S.R., Hu, X., Martini, A., Jacobs, T.D.B.: Matching Atomistic Simulations and In Situ Experiments to Investigate the Mechanics of Nanoscale Contact. Tribol. Lett. 67, 97 (2019). Copyright © 2019, Springer Nature.

was neglected because its accurate inclusion would require knowledge of the precise location of the tip contact – including in the out-of-plane direction – which cannot be identified with sufficient precision due to the finite resolution in the TEM. Fixed boundary conditions were applied in all directions.

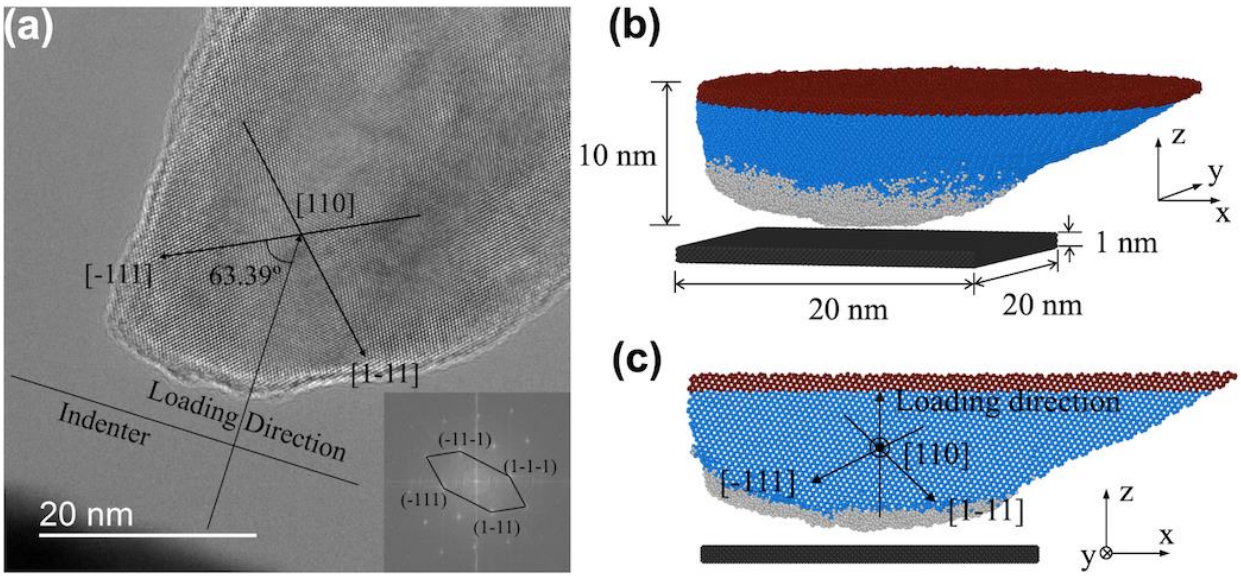

Figure 14. A high-resolution TEM image (a) of the AFM tip is shown with crystallographic and loading directions labeled. The inset image shows the 2-D Fourier transform of the corresponding TEM image. The atomistic model is shown in perspective (b) and cross-sectional (c) views. Sphere color represents atom type, where: blue is crystalline silicon; silver is amorphous silicon; red is the rigid part of the tip; and black is carbon. Figure reproduced with permission from Ref. [101].

The modified Tersoff potential [142], which is known to be able to accurately capture the mechanical properties of silicon, was employed to simulate the interactions within the silicon tip. The interactions between tip and substrate were modeled by the Lennard-Jones potential with the addition of a Buckingham potential to capture the large short-range adhesive interactions that were

observed in the experiment. Contact area in the simulation is calculated as described in Sect. 3.4 and Fig. 4.

The probe was moved towards the substrate until it reached the maximum force observed from experiment. After the probe reached the maximum force, it was relaxed for 0.7 ns to ensure stability in energy and force. After relaxation, the probe was retracted from the substrate at 5 m/s to simulate an unloading process. Due to realistic limitations of computation time, the loading and unloading speeds were significantly faster than experiment. However, contact mechanics models do not predict an effect of pull-off speed for hard, non-viscoelastic materials. Further, long-timescale processes such as creep are not expected to play a significant role in the present contact. To verify this, we repeated the simulations at speeds ranging from 0.2 to 10 m/s and observed no statistically significant effect on pull-off force.

6.1.2 Matching Adhesive Interactions between Simulations and Experiments

To ensure that the simulations and experiments were describing the same nanocontact, it was necessary to match the adhesion strength at the interface, as quantified by the pull-off force. The force-vs-time data from experiment is shown in Fig. 15a where the maximum displacement of the AFM probe corresponds to the maximum force of 408 ± 31 nN achieved in the test. The pull-off force is the amount of force required to break the contact; in this case it was found to be 434 ± 31 nN.

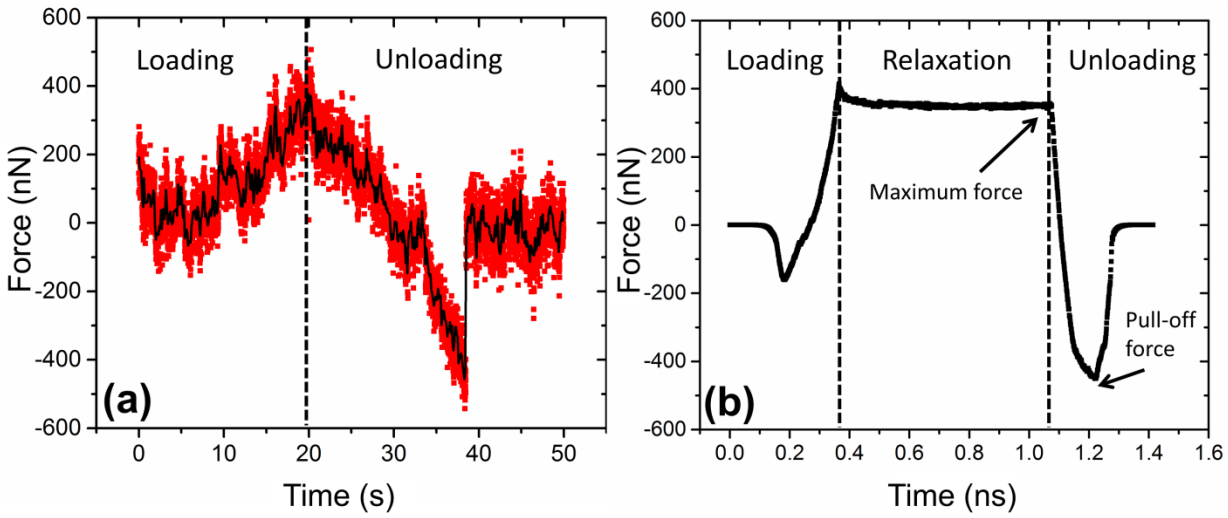

Figure 15. The force as a function of time from experiment (a), shown as both raw (red symbols) and downsampled (black line) data, and from simulation (b). As shown, the maximum and pull off forces are matched between experiment and simulation, while the timescales differ significantly. Figure reproduced with permission from Ref. [101].

In the simulations, the adhesive interactions between the atoms in the two surfaces were described using the sum of the Lennard-Jones and Buckingham forces. The Lennard-Jones potential approximated the van der Waals attraction and Pauli repulsion between the materials, and the parameters were set as ε = 0.0024 eV, σ = 0.28 nm [100]. The relatively large adhesion observed in the experiment was likely due to the formation and breaking of covalent bonds during the test. Covalent bonding could be modeled explicitly in the simulation using a reactive potential, but this approach would severely limit the size of the system. Therefore, an approximation was introduced that captured the adhesion in an effective way for a sufficiently large model system. Specifically, the Buckingham potential was used to add an additional attractive force between the tip and the substrate [143, 144]. The Buckingham potential has the form $E = -\alpha e^{-r/\zeta}$, where α is the maximum attractive energy between two atoms, and ζ is the characteristic short-range decay

length. The value of ζ was set to be 0.3 times the value of σ of the Lennard-Jones potential [143, 144]. The pull-off force increased approximately linearly with the magnitude of the parameter α, and the experimental pull-off force was reproduced in the simulation using a value of α = 3.5 eV. This extracted Buckingham parameter α is comparable to the energy of a silicon-carbon bond, which is 3.3 eV [145]. The simulation force-vs-time data is shown in Fig. 15b. The maximum force and the pull-off force in the simulation were 367 ± 2 nN and 457 ± 8 nN, respectively.

6.1.3 Measurement of Work of Adhesion for Silicon Diamond Nanocontact

To determine the work of adhesion from the experiment, the method of Ref. [22] was used. Specifically, three steps were performed: (1) evaluate the geometry of the body to confirm a parabolic shape and measure tip radius; (2) compare the shapes of the bodies before and after contact to confirm that there was no change in overall shape due to testing; and (3) determine which of the continuum contact models is predicted to apply by computing the Tabor parameter for the contact.

To evaluate the geometry of the bodies, the outer contour of the probe was traced using image analysis. To verify near-parabolic shape (Step 1), the traced contour was fit to a parabola of the form $z = x^2/2R$, where z is the vertical height, x is the lateral dimension, and R is the radius. To assess changes with testing (Step 2), the traced contours were compared before and after testing. Before testing, the probe radius was 20.0 $\pm$ 1.8 nm (Fig. 16a) and the root-mean-square (RMS) deviation from the paraboloidal shape was 0.17 nm. After testing, the probe radius was 20.7 $\pm$ 1.4 nm (Fig. 16b) with an RMS deviation of 0.16 nm. While there were Angstrom-scale modifications to the probe, the probe remained paraboloidal and the radii were indistinguishable

within experimental uncertainty. The geometric assessment supports the application of classical contact mechanics models.

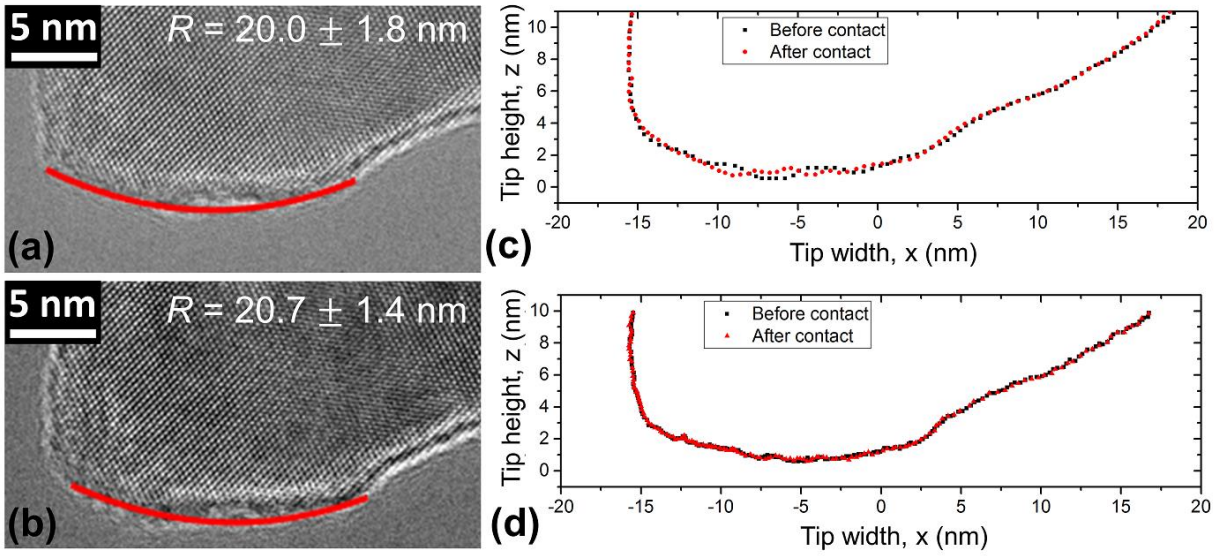

Figure 16. TEM images of the probe (a) before and (b) after contact with best fit parabolas shown in red. Probe profiles are compared in the experiment (c) before and after contact and in the simulation (d) before and after contact. These results confirm a lack of permanent shape change due to plasticity or fracture. Figure reproduced with permission from Ref. [101].

To determine which of the contact models is predicted to apply (Step 3), the Tabor parameter was computed using Eq. 2-8. This required first obtaining the work of adhesion, which was calculated from Eq. 2-10 using the measured adhesive force, and probe radius. The work of adhesion computed for the diamond and silicon pair was found to be in the range of 3.3 ± 0.2 J/m^2 (DMT) and 4.4 ± 0.3 J/m^2 (JKR). The effective modulus for silicon diamond nanocontact was 126.9 GPa, which was computed using the elastic properties of [1 0 0] diamond (E = 1050.0 GPa, ν = 0.1) [146] and silicon, oriented along the loading direction. The properties

of the silicon were E = 132.8 GPa and $\nu = 0.28$, which were obtained from elastic constants C_{11} = 165.6 GPa, C_{12} = 63.9 GPa, C_{44} = 79.5 GPa [147] and a loading direction of $[2\ \bar{2}\ 19]$. Using the procedure described in Sect. 2.1, with a range of adhesion of 0.2 – 0.3 nm [22, 30, 100, 148, 149], the Tabor parameter was found to be $\mu_T = 0.8 - 1.5$ and the work of adhesion was found to be 4.2 ± 0.4 J/m^2. This indicates that the contact lies in the transition region between the JKR and DMT limits, and should be described using the Maugis-Dugdale model.

The measured work of adhesion was larger than previous measurements. While prior *ex situ* testing of diamond/diamond, silicon/silicon, and diamond/silicon contacts have yielded W_{adh} = 0.1 – 0.7 J/m^2 [23, 100, 109, 150–152], prior *in situ* TEM testing [153] of a silicon/diamond contact demonstrated significantly higher work of adhesion values, due to bonding across the interface and changing interfacial roughness, both of which are modified by loading of the contact. The work of adhesion for an ideally bonded contact can be computed [14] as the product of the areal density of bonds and the bond energy. Using minimum and maximum surface bond densities of approximately 6.8×10^{18} atoms/m^2 and 9.6×10^{18} atoms/m^2 (calculated from the surface atom density of silicon in the orientations $[1\ 0\ 0]$ and $[1\ 1\ 0]$ respectively) and a bond energy of 318.0 kJ/mol [145], the covalent work of adhesion is $3.6 - 5.1$ J/m^2 between silicon and diamond. Therefore, the measured work of adhesion is commensurate with covalent bonding across the interface.

6.1.4 Measurement of Contact Area as a Function of Force

The contact area and deformation as functions of applied force are shown in Fig. 17. Experimental and simulated measurements for the area of contact agree within the uncertainty of the measurement. The uncertainty of the experimentally measured values arose due to vibration of

the *in situ* indenter. For deformation, the experiments and simulations agree for the adhesive region only, and differ by more than experimental uncertainty for the compressive region. This difference at high loads may arise due to the finite size of the simulated tip, where the presence of the rigid layer artificially stiffens the contact.

Both the experiments and simulations demonstrate hysteresis in behavior between the loading and unloading portions of the tests. The contact area at zero applied force is larger upon unloading by 88% (in experiments) and 110% (in simulations) as compared to the same value measured during loading. This hysteresis behavior is not predicted by continuum elastic models. While this can be a hallmark of permanent changes within the material, there is no gross shape change observed before/after testing, as discussed in the Sect. 6.1.3.

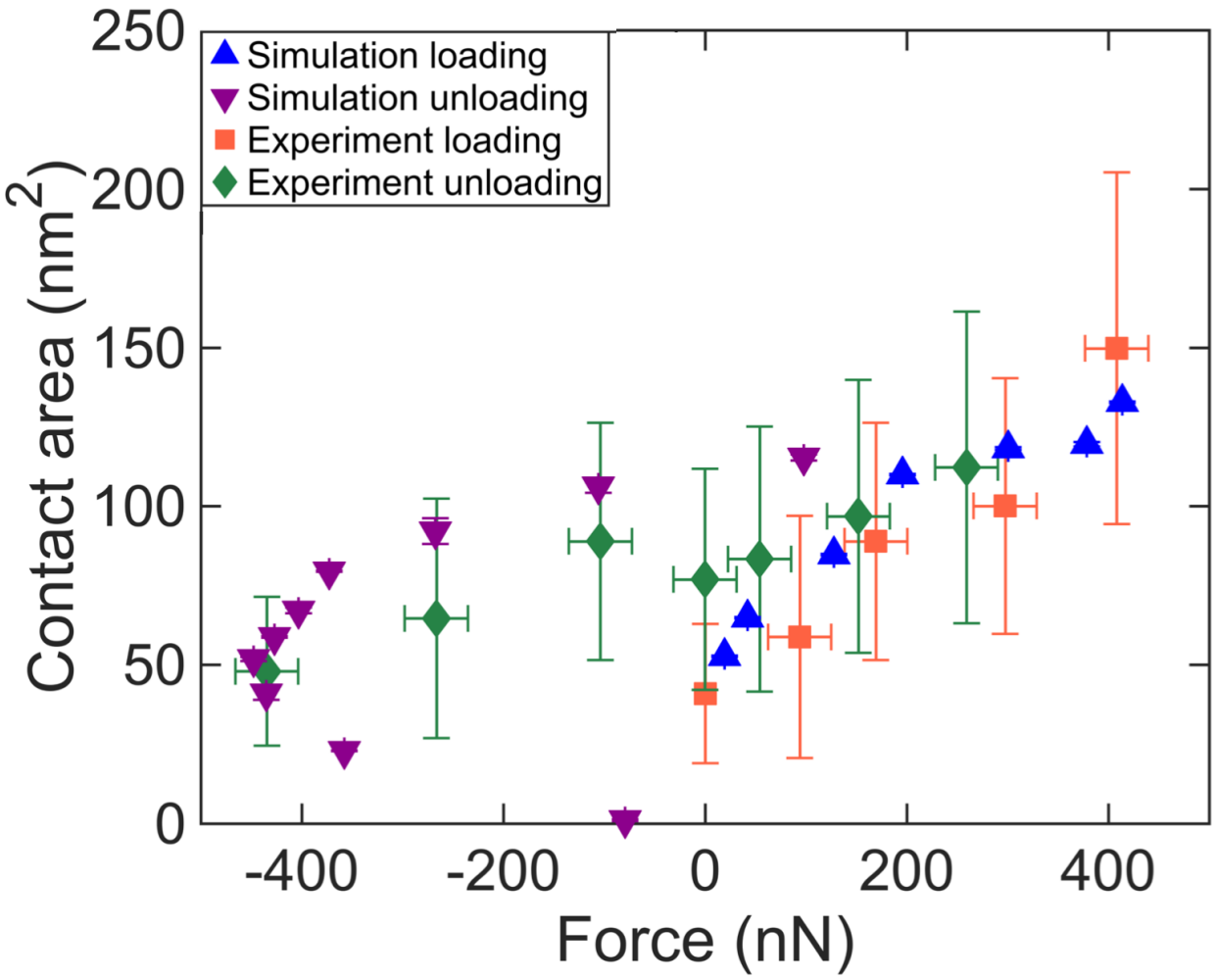

Figure 17. Contact area (a) as a function of applied normal force, from experiment (squares) and simulation (triangles). Figure reproduced with permission from Ref. [101].

6.1.5 Quantifying the Hysteresis in Contact Area: Increasing Work of Adhesion as a Function of Maximum Stress

None of the contact mechanics models (JKR, DMT, Maugis-Dugdale) could capture the hysteresis between loading and unloading behavior; therefore these two segments were investigated independently. The simulated unloading curve could be accurately fit using the intermediate case of Maugis-Dugdale with an effective modulus of 96.8 GPa (free parameter) for a transition parameter $\lambda = 1.6$ and work of adhesion of 4.4 J/m^2 (λ and W_{adh} are simultaneously solved from the measured pull-off force and the best-fit E^* using the numerical analysis provided by COS method [20]. The experimental unloading curve was accurately fit also using the Maugis-Dugdale theory, with $E^* = 126.0$ GPa (free parameter) for $\lambda = 1.3$ and $W_{adh} = 4.3$ J/m^2. The above analysis assumed an equilibrium separation $z_o = 2.5$ Å. Repeating this analysis using values in the range of 2.0 Å – 3.0 Å resulted in small changes of the best-fit effective modulus ($\pm$ 5.2% for experiment, and $\pm$ 5.7% for simulation). The extracted best-fit value for effective modulus from the experiment matches well with that of crystalline silicon, which is 126.9 GPa as computed in the Sect. 6.1.3.

By contrast, the Maugis-Dugdale model with the same parameters overestimated the contact area upon loading by 51%. Indeed, the loading portion of the curve could not be accurately fit for any value of E^*. Therefore, the fit was retried allowing for a variable work of adhesion. Specifically, W_{adh} was allowed to vary with force, while the radius was held constant at the measured value (20.7 nm) and the effective modulus was held constant at the best-fit value determined in the previous paragraph (111.4 GPa, the average of the experimental and simulated best-fit values). Figure 18a shows the measured data, alongside curves representing the Maugis-Dugdale model with varying works of adhesion. Figure 18b shows the extracted best-fit work of

adhesion at each value of the stress in the contact. This best-fit value increases monotonically from 1.3 J/m^2, which accurately fits the contact area and force at the initial point, to 4.3 J/m^2, which fits well the contact area and force for the unloading data.

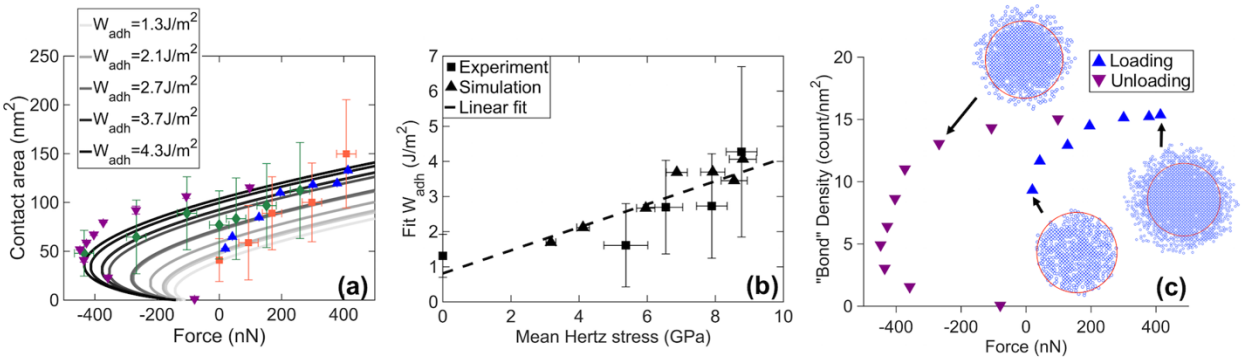

Figure 18. The data for contact area versus force (a) has been fit using the Maugis-Dugdale model with varying work of adhesion. The effective modulus was set using the best-fit value of 111.4 GPa for unloading, and the work of adhesion is varied to separately match each individual point in the loading curve. The result of this point-by-point fit (b) shows a monotonically increasing value of work of adhesion with increasing mean Hertz stress. The meaning of the symbols in (a) are the same as described in Fig. 17. The simulation results were used to compute the areal density of in-contact atoms (c) in the central region of contact (red circle). The initial contact area shows a lower density of "bonds", which increases monotonically throughout loading. Notably, the high final "bond" density is maintained during unloading to large negative forces. Figure reproduced with permission from Ref. [101].

The variation between properties measured during loading and unloading has been observed in a variety of materials and is often referred to as *adhesion hysteresis* [14]. This effect is traditionally attributed to capillary effects [154] or to viscoelasticity in soft materials [155, 156], or to plasticity in hard materials [157]. Because the present test was performed in a vacuum

environment, using hard non-viscoelastic materials (silicon and diamond), capillarity and viscoelasticity can be ruled out. Further, unlike in traditional AFM testing, the *in situ* TEM images and the MD simulations were used to rule out significant shape change upon testing. Atomic-scale plasticity of the type shown in Ref. [153] was not observed, likely because no sliding was induced and the tip had been pre-loaded to higher loads before these experiments were conducted. Therefore, it is expected that inelastic deformation would have already taken place prior to the present test. Instead, in these silicon/diamond contacts, the origin of the adhesion hysteresis is understood to be covalent bond formation, as discussed in Ref. [153]. As described in that work, this is equivalent to using continuum contact mechanics with a modified W_{adh}, which depends on loading conditions, including the amount of pre-load and speed of lateral sliding. The physical origin of these changes in W_{adh} are increased covalent bond activity from stress in the contact.

Further insight is obtained by combining the *in situ* experiments with the MD simulations to examine atomic-scale interactions in the contact interface. Specifically, a measurement was taken of the areal density of in-contact atoms, identified using the force criterion. This is loosely analogous to a bond density; however, in the absence of a reactive potential, the concept of a "bond" is not well-defined. For a fixed central region of the contact, this areal density was measured at various points throughout the test, and is shown in Fig. 18c. The result demonstrates a monotonic increase from the initial value to the value at the highest force. In other words, for a given area of contact, the additional loading has pushed a larger number of atoms into close contact and thus into the deepest part of the interatomic potential. Therefore, this region of contact will require more energy to separate, thus corresponding to a larger work of adhesion in a continuum description. Indeed, the high density of in-contact atoms achieved at the maximum force (400 nN) was maintained (within 10%) throughout unloading, all the way to the point where a tensile force

of approximately 270 nN was applied. Overall, the 65% increase in "bond" density during loading does not fully explain the measured increase in work of adhesion; however, the qualitative trends are similar. Therefore, the present results further elucidate the adhesion hysteresis that arises due to stress-dependent bond formation across the interface.

6.1.6 Conclusions

This investigation comprised a comprehensive analysis of the loading and separation of a nanocontact using experiments and simulations. First, the experimental and simulated measurements for contact area as a function of applied force demonstrated hysteretic behavior, with larger values measured upon unloading as compared to loading. Therefore, they could not be accurately fit using a straightforward application of continuum mechanics via the Maugis-Dugdale model. The Maugis-Dugdale model *could* be accurately fit to the unloading portion of the contact area curve with a reasonable value of effective elastic modulus extracted from the fit; however, the same model over-predicted contact area by an average of 51% during loading. Third, a significantly better fit to contact area was found by allowing the work of adhesion to increase with applied force from 1.3 to 4.3 J/m^2. Traditional explanations for adhesion hysteresis, including viscoelasticity, capillarity, and plastic deformation, were ruled out using *in situ* observation of geometry and materials in the contact. Rather, variable work of adhesion due to stress-dependent covalent bond formation across the interface was confirmed and further elucidated by atomic-scale observation of the simulated contact and the increase in areal density of in-contact atoms.

6.2 Quantifying the Increase of Work of Adhesion with Applied Stress for Silicon Diamond Nanocontacts[10]

6.2.1 Experimental and Simulation Contact Tests on Silicon Diamond Nanocontact

A combined total of 77 single-asperity adhesion tests at varying loads were conducted using *in situ* TEM and molecular dynamics simulations. Experimental tests were performed as described in the Sect. 3.1 with direct TEM observation and also with the beam off, in order to rule out electron-beam artifacts. A series of more than 50 tests were performed with varying probe radius in the range of 10-40 nm and applied forces in the range of 0-800 nN.

In order to capture the bonding across the interface, atomistic simulations of silicon diamond nanocontact were performed using ReaxFF potential [158]. A schematic of the atomistic model is shown in Fig. 19a and a representative force-time curve is shown in Fig. 19b. A parabolic silicon probe was created with a radius of 3 nm and was fully terminated with hydrogen. All interactions were modeled by the ReaxFF potential [158] with the parameter set from Ref. [159] using a time step of 0.25 fs. The normal force was calculated as the sum of the forces on the probe atoms [47]. The probe was moved towards the substrate at 5 m/s until it reached the desired force, was held at this position until the energy reached steady state, and then was retracted from the substrate at 5 m/s. The simulation loading/unloading speed was much faster than that in the

[10] Much of this section appears in print: Adapted with permission from Chen, R.*, Vishnubhotla, S.B.*, Khanal, S.R., Jacobs, T.D.B., Martini, A.: Quantifying the pressure-dependence of work of adhesion in silicon-diamond contacts. Appl. Phys. Lett. 116, 051602 (2020). Copyright © 2020, AIP Publishing. *Indicates equal contribution.

experiments due to the small time-step required by the atomistic simulation method. The maximum forces in the simulation ranged from 3 to 150 nN, resulting in a range of mean applied pressures from 3 to 11 GPa, consistent with the applied pressures in the experiments.

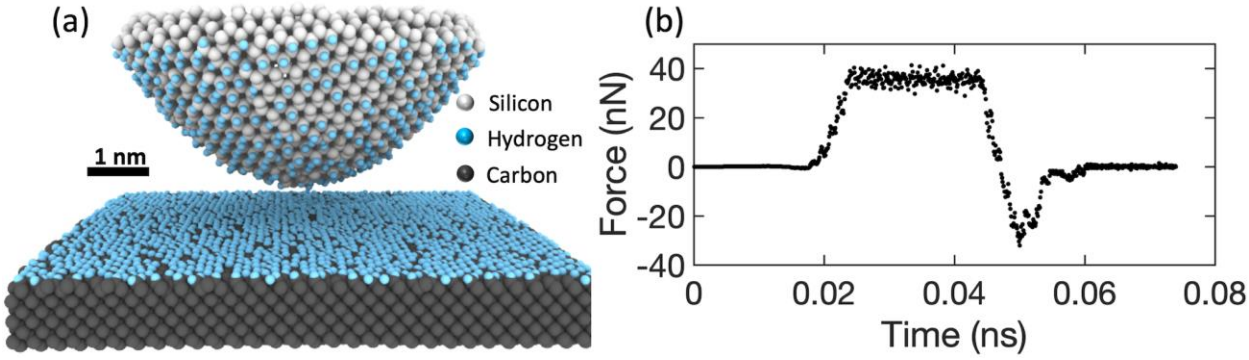

Figure 19. The adhesion tests was performed on silicon diamond nanocontact using atomistic simulations. A paraboloidal silicon probe of 3 nm radius was moved towards a flat diamond substrate (a) to measure force during loading and pull-off (b). Figure reproduced with permission from Ref. [104].

6.2.2 Work of Adhesion Increases with Mean Applied Stress for Silicon Diamond Nanocontact

The Maugis parameter λ was calculated using Eq. 2-9 for all the experiment and simulation tests to determine which contact model is applicable for silicon diamond nanocontact. The equilibrium separation z_0 is 0.25 nm [22, 30, 100, 148, 160] and the effective modulus E_{eff} is 124.5 GPa, calculated from the elastic modulus of [1 0 0] diamond (E = 1050.0 GPa, ν = 0.1) [146] and [1 0 0] silicon (E = 130 GPa, ν = 0.28) [147]. The radius R for multiple silicon AFM probes was measured before and after all tests from high-resolution TEM images (Fig. 20).

Using these values of z_0 and E_{eff}, and the vales of F_{adh} and R measured in the experiments and simulations, the COS method was applied to simultaneously measure the Maugis parameter λ and work of adhesion W_{adh} for all the tests. It was observed that the Maugis parameter λ lies in the range of $0.23-1.56$, thus representing an intermediate case between the DMT and JKR limits. All reported work of adhesion values were subsequently determined based on this implementation of the Maugis-Dugdale model.

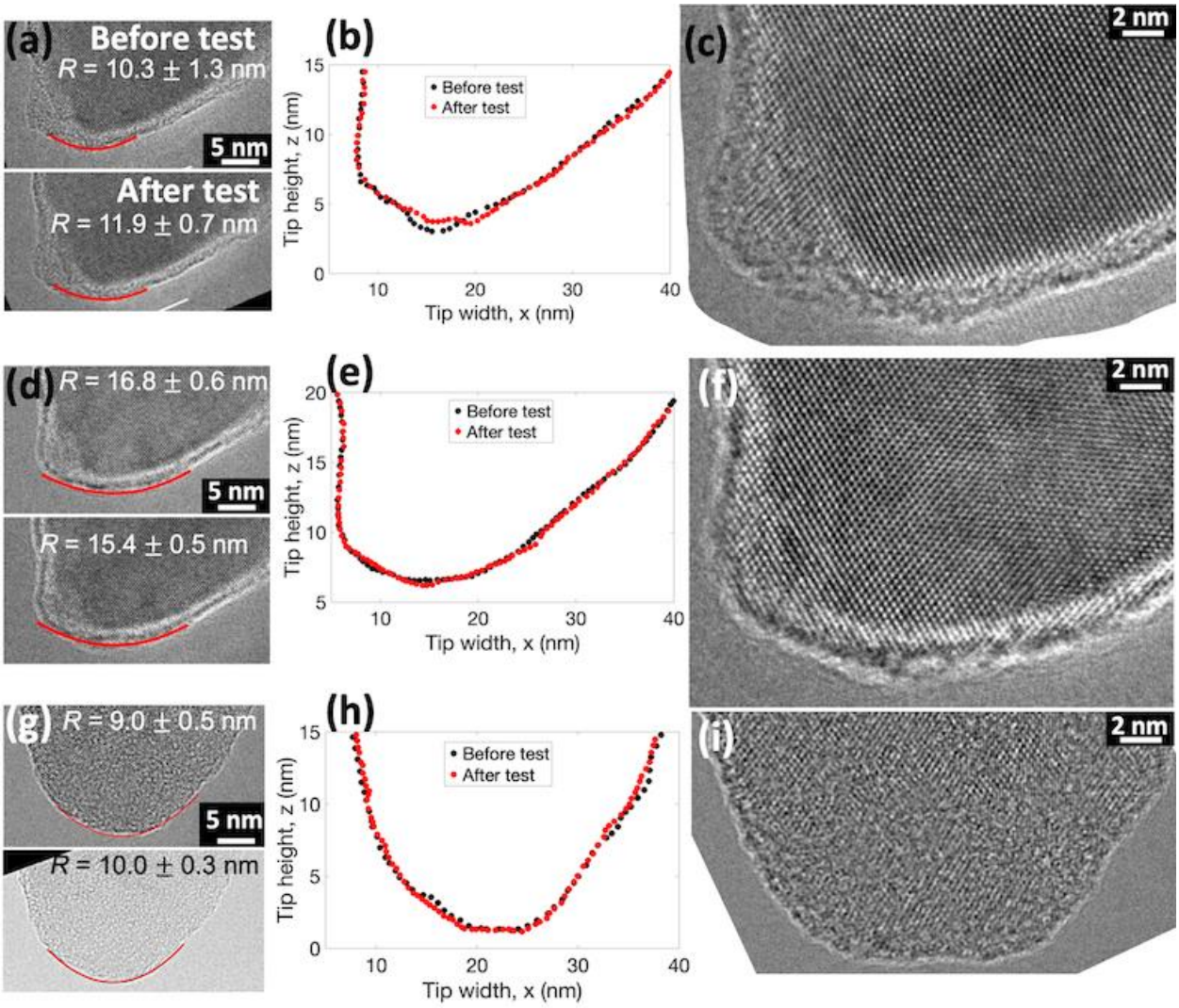

Figure 20. High-resolution TEM images were taken before and after the test for multiple probes (Probe 1: a-c, Probe 2: d-f, Probe 3: g-i) to determine probe radius, shape, and crystal structure. The TEM images were used to trace the outer profile of the probe and fit a parabola to measure the apex radius. For all the probes, there was no significant change in the radius or shape (b,e,h). TEM images of the probes after the test show no evidence of the defects in the silicon lattice (c,f,i). Figure reproduced with permission from Ref. [104].

The mean applied stress p_m at the maximum applied force F_{max} for a given probe of radius *R* was calculated using an elastic-plastic model Kogut and Etsion [118] for the contact of spheres. In this, the standard, elastic Hertz model is used up to the point where local yielding is predicted; beyond this point, an empirically derived relationship is used to predict contact pressure.

The elastic-plastic model is an extension of the Hertz model, to describe behavior after the body is predicted to exhibit local plastic deformation. In this model, the transition from the elastic to elastic-plastic (yielding inception) occurs at the critical interference (deformation) ω_c. At the transition, the critical stress p_c is calculated as $p_c = \frac{2}{3}KH$, where *H* is the hardness, *K* is a hardness coefficient that is calculated as K=0.454+0.41ν, and ν is the Poisson Ratio. For silicon, which has a Poisson ratio of 0.28 and a hardness of 13 GPa [161], the calculated critical pressure is 4.9 GPa.

Using the Hertz model, the normalized interference (ω/ω_c) can be related to the normalized stress (p_h/p_c) by [118]:

$$\frac{\omega}{\omega_c} = \left(\frac{p_h}{p_c}\right)^2 \tag{6-1}$$

The mean Hertz stress p_h at the maximum force F_{max} for a given probe radius *R* is given by [162]:

$$p_h = \frac{2}{3}\left(\frac{6F_{max}E^{*2}}{\pi^3 R^2}\right)^{1/3} \tag{6-2}$$

For $\frac{\omega}{\omega_c} < 1$, the applied stress is less than the critical stress (4.9 GPa), and the contact is purely elastic. In this case, the mean stress p_m is given by the mean Hertz stress (Eq. 6-2). For applied

stresses greater than 4.9 GPa, the contact transitions into elastic-plastic and the mean stress is given by the following empirical equations [118]. For $1 \leq \frac{\omega}{\omega_c} \leq 6$, which corresponds to the prediction of the local yielding just below the surface with the contact being elastic, the mean stress is given by [118]:

$$p_m = 1.1075 \times p_c \times \left(\frac{\omega}{\omega_c}\right)^{0.289} \tag{6-3}$$

For $6 \leq \frac{\omega}{\omega_c} \leq 110$, which corresponds to the global yielding with the contact area being elastic-plastic for $6 \leq \frac{\omega}{\omega_c} \leq 68$ and fully plastic for $68 \leq \frac{\omega}{\omega_c} \leq 110$, the prediction for the mean stress is given by [118]:

$$p_m = 1.4894 \times p_c \times \left(\frac{\omega}{\omega_c}\right)^{0.1170} \tag{6-4}$$

The results from 77 adhesion tests are shown in Fig. 21. Together, the experimental and simulation data show an increase in work of adhesion from approximately 1 J/m^2 at zero applied pressure up to 6-8 J/m^2 at high pressures. The increase is gradual at low pressures where deformation is expected to be elastic and then increases rapidly at the higher pressures of elastic-plastic deformation. The results at zero applied pressure agree well with those of Ref. [153], in which sliding and pull-off experiments were conducted under the action of adhesive stress only. Simulations performed in that study with silicon probes and diamond surfaces showed that larger loads increased smoothing of the probe and interfacial covalent-bond formation, both of which

increase adhesion. The present results show that the work of adhesion continuously increases with applied pressure up to very high values.

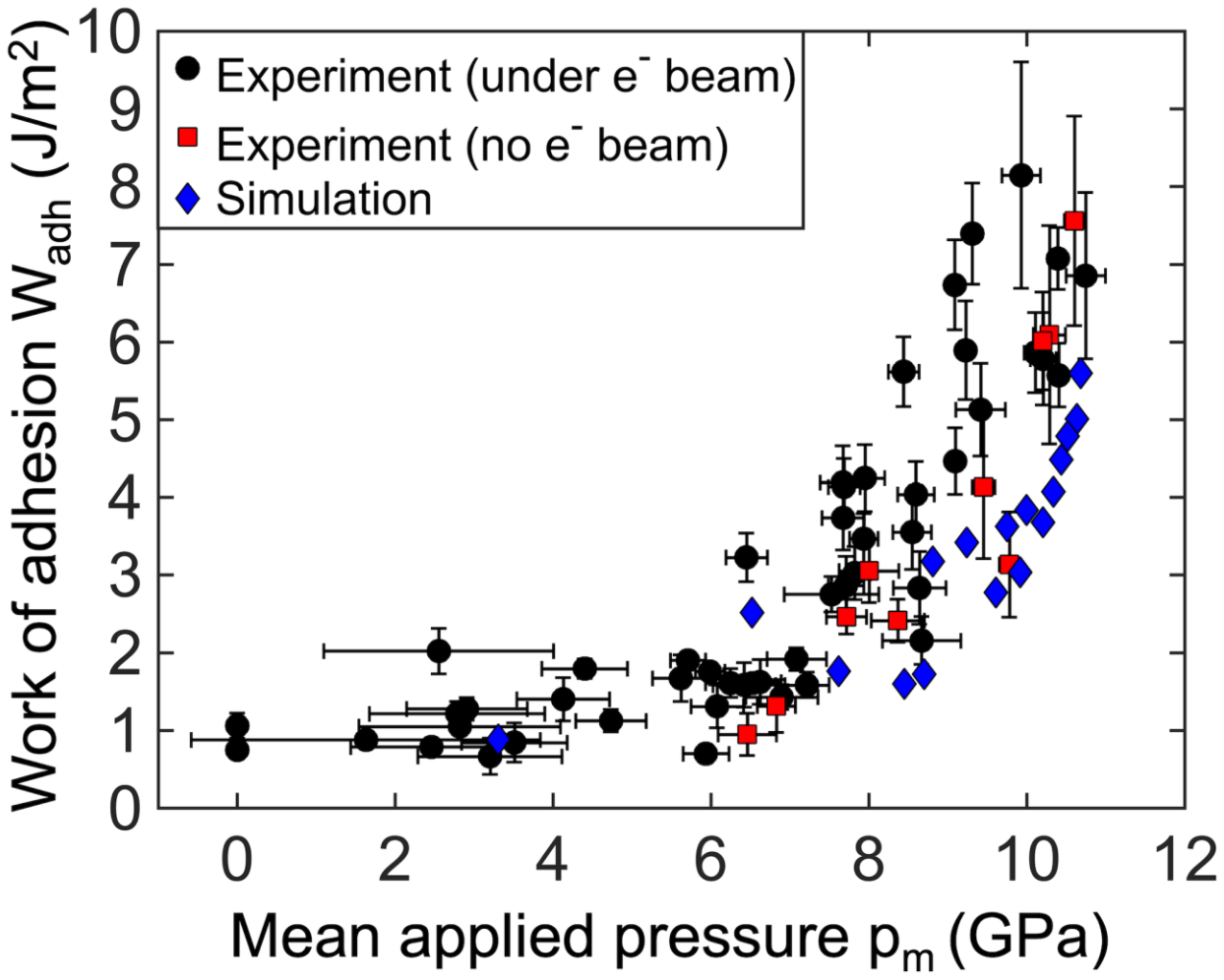

Figure 21. The measured work of adhesion from experiments and simulations increases approximately seven-fold with applied pressure, where the most significant increase occurs above 5 GPa. The work of adhesion is calculated using the Maugis-Dugdale model; the mean applied pressure is calculated using an elastic-plastic model of contact (see main text). Experimental tests were performed with direct TEM observation (black symbols) and also with the beam off (red symbols), in order to rule out electron-beam artifacts. Figure reproduced with permission from Ref. [104].

6.2.3 Work of Adhesion Increases with Mean Applied Stress for Varying Hydrogen Coverages

Previous work on nanoscale diamond contacts showed that the work of adhesion depends on the hydrogen coverage [152, 153, 163, 164]. Because the termination of the experimental surfaces was unknown, the flat diamond substrate was investigated at hydrogen coverages ranging from 0 to 100%.

Simulated testing with varying hydrogen coverages and other probe sizes (Fig. 22) show that, while the absolute values of work of adhesion vary between conditions, the trends of increasing work of adhesion with applied pressure are consistent across all model contacts. A coverage of 85% was chosen for this study to best match the experimental results in terms of the magnitude of the work of adhesion (Fig. 21).

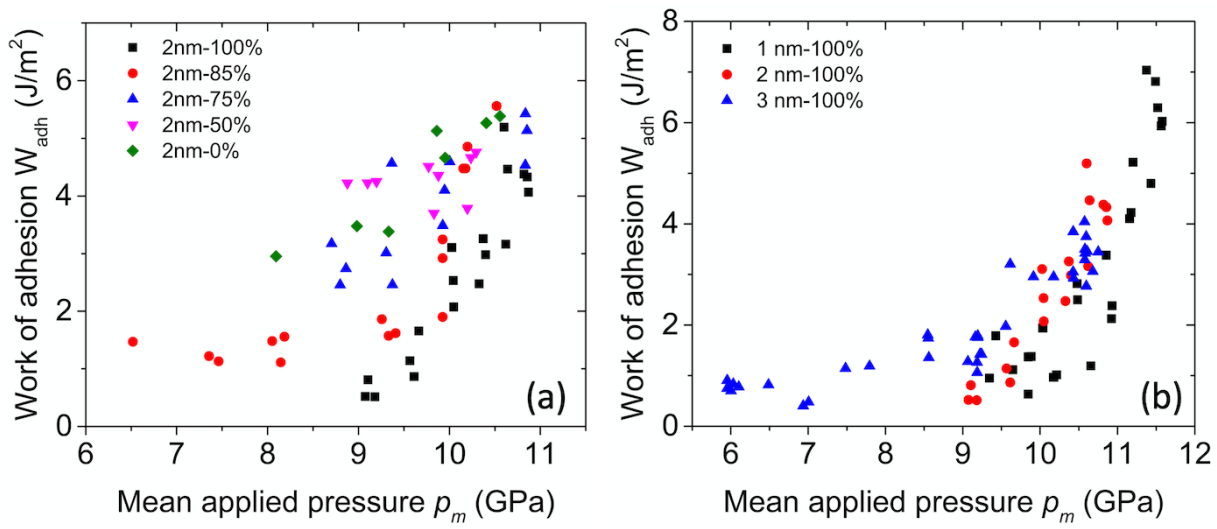

Figure 22. The work of adhesion from the simulation varied with increasing hydrogen coverage (a), consistent with prior results [164], but data from all coverages exhibited increasing trends with applied pressure. Work of adhesion was also measured with three different probe sizes (b) with a hydrogen coverage of 100% and the trends in work of adhesion were again consistent. Figure reproduced with permission from Ref. [104].

6.2.4 The Increase in Work of Adhesion is due to Modification of Atomic-Scale Interactions with Loading

These results demonstrate a significant increase in work of adhesion with applied stress. To support that these changes arise from atomic bonding, rather than other physical origins, we sought to rule out three other common explanations for varying adhesion, including: electron-beam induced reactions [165]; shape change by inelastic deformation [157] (such as fracture or gross plastic flow); and time-dependent deformation [154–156] (such as viscoelasticity or creep).

First, to investigate the effect of the electron beam, TEM experiments were conducted with the electron beam switched off (red markers in Fig. 21). The measured work of adhesion still

increased with applied pressure, agreeing with the beam-on measurements (black markers in Fig. 21) within the experimental uncertainty. Further evidence that the electron beam did not have a strong effect is provided by post-hoc analysis of beam current during beam-on testing, which demonstrated that deviations in electron dose rates during testing (over the range of 96-317 e^-/A^2s) had no systematic effect on adhesion results. Consistent with prior results showing that silicon probes are robust to electron beam exposure [166], the present experiments showed no evidence of contamination or damage of the probe due to the electron beam.

Second, while large-scale shape change from inelastic deformation (fracture or gross plastic flow) could potentially lead to an increase in contact size and therefore adhesive force, this was ruled out by examining the probes before and after testing. From side-view images of the probes, the exterior profile was extracted and a parabola was fit to the probe's apex (see Fig. 20). For all cases, the average change in radius of the probe apex was just 1%, with no single radius deviating by more than 9% from the pre-test value. To assess any smaller-scale changes, the best-fit parabola was subtracted from the measured profile leaving only the sub-nm-scale roughness. In all cases, the roughness was approximately equivalent before and after testing: the average change in root-mean-square (RMS) roughness of all the probes was 1%, with no single value of RMS roughness deviating by more than 9% from the pre-test value. Furthermore, high-resolution images of the probes taken immediately after testing (Fig. 20c,f,i) showed no evidence of dislocations or other defects in the crystal lattice. A similar analysis performed on the simulated probes by tracking atom positions showed no evidence of a change in probe shape or crystal defects.

Third, the order of the tests was varied, including repeating multiple tests to the same load and conducting a lower-load test following a higher-load test (Fig. 23). It is expected that inelastic material changes will occur when the probe is subjected to a previously unachieved load, but would

be less significant upon subsequent testing to a similar or lower load. To see if this is occurring, multiple adhesion tests were conducted on a silicon probe of radius 22.7 nm to measure adhesive force for different maximum applied forces. As shown in Fig. 23, Test 1 was conducted at the maximum load of 356 ± 31 nN, which had an adhesive force of 306 ± 31 nN. Then, test 2 was conducted at a lower maximum load of 186 ± 31 nN, which resulted in a smaller adhesive force of 188 ± 31 nN. Next, tests 3, 4 and 5 were conducted to the same maximum load of approximately 400 nN. These repeated tests have a similar adhesive force of approximately 430 nN. By contrast, these variable and repeated measurements on the single probe suggest that the order of testing does not affect the adhesive force, and shape change by inelastic deformation plays a limited role in these contacts.

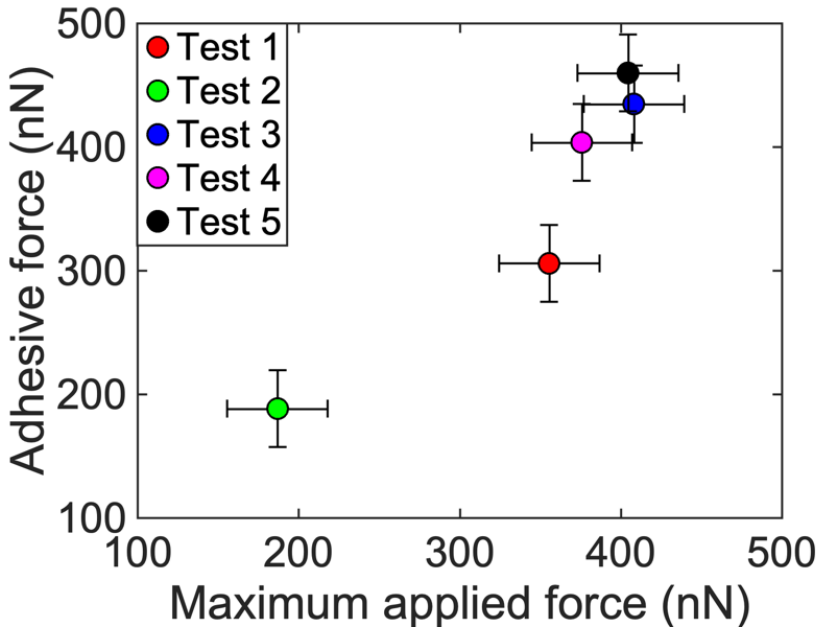

Figure 23. Multiple adhesion tests on the silicon probe show that the order of testing does not affect the adhesive force. The increase in work of adhesion with applied pressure is not due to shape change by inelastic deformation. Figure reproduced with permission from Ref. [104].

Finally, to rule out time-dependent phenomena such as creep or viscoelasticity, the adhesion tests were repeated with variation in hold time and pull-off rate. The experimental tests were conducted for five different hold times between 0 to 60 s at a maximum force of 417 $\pm$ 40 nN with a probe radius of 21.9 $\pm$ 1.5 nm. Similarly, simulation tests were conducted for different hold times from 2 to 12 ns at three maximum forces of 132.2 $\pm$ 2.0 nN, 21.8 $\pm$ 0.8 nN, and 2.2 $\pm$ 0.4 nN. The adhesive force showed no significant trends with hold time in both experiments (Fig. 24a) and simulations (Fig. 24b). In experiments on a different probe (radius 41.0 $\pm$ 7.2 nm), three contact tests were conducted with an applied maximum force of 197 $\pm$ 34 nN and pull-off rate of 0.5, 1, and 2 nm/s. The pull-off force did not show any significant change with unloading rate in the range of 0 to 2 nm/s (Fig. 24c). In the simulations, the rate of pull-off was varied from 2 to 10 m/s and there was no notable change of the adhesive force (Fig. 24d). Therefore, the tested range of hold times and speeds had no effect on measured adhesion and cannot explain the increase of work of adhesion with applied stress.

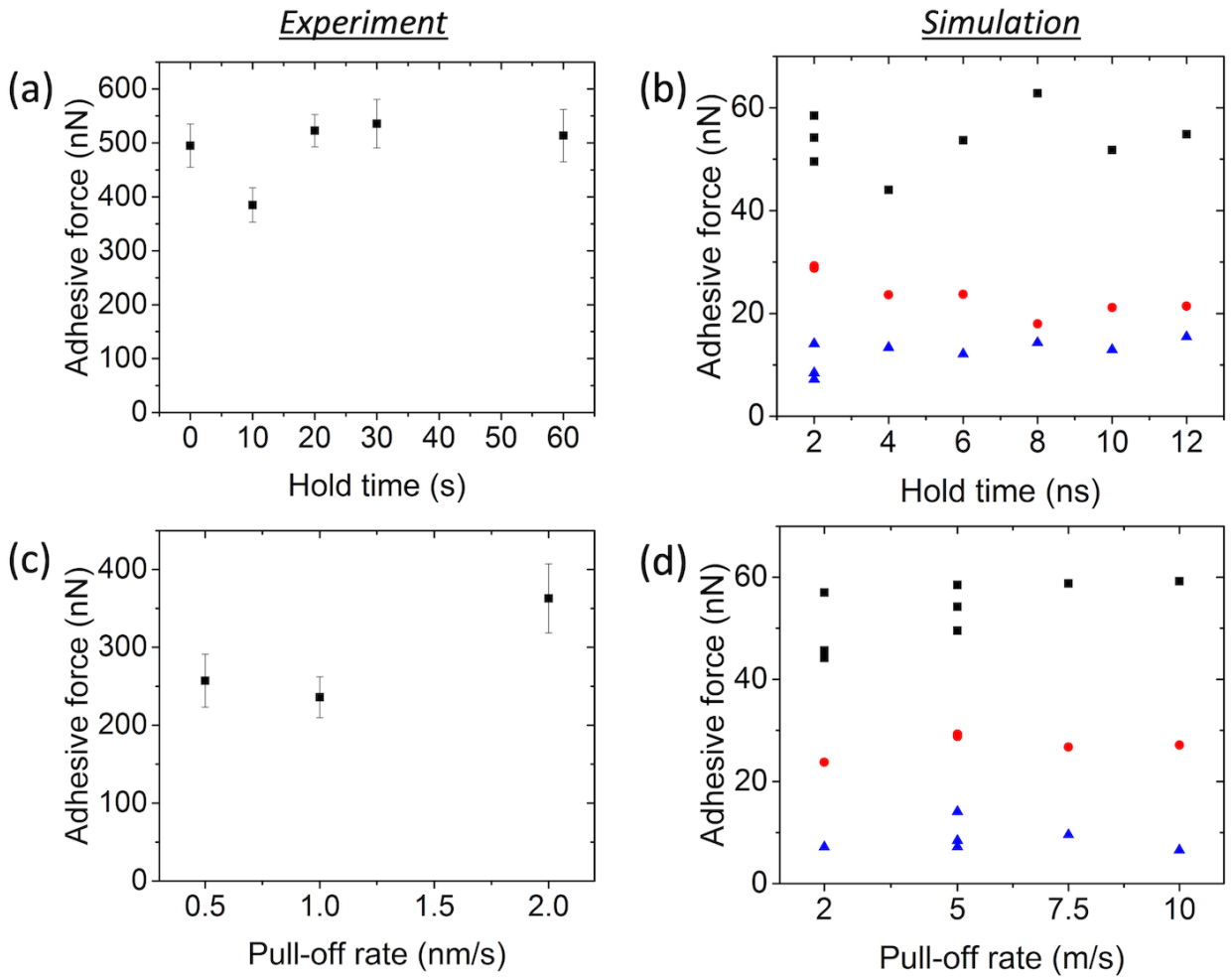

Figure 24. The increase in work of adhesion with applied stress cannot be attributed to time-dependent phenomena such as creep or viscoelasticity. In both experiments (a,c) and simulations (b,d), the adhesive force shows no dependence on hold time nor on pull-off rate within the limits explored. In (b) and (d), the black squares, red circles, and blue triangles refer to maximum applied forces of 132 nN, 21.8 nN, and 2.2 nN, respectively, for a probe radius of 3 nm. Although the timescales of the experiment and simulation differ significantly, these plots confirm that the adhesive force does not depend on the hold time or pull-off rate within the range of times and rates accessible to each method. Figure reproduced with permission from Ref. [104].

After ruling out the possible effects of three common explanations for varying adhesion—electron-beam induced reactions, shape change by inelastic deformation, and time-dependent deformation—the present results are attributed to chemical bonding across the interface that is facilitated by stress as suggested by prior experiments and MD simulations [101, 153]; we show that these trends continue and are accelerated with applied stress. Specifically, the increase in measured work of adhesion corresponds to a stress-driven increase in interfacial bond density, requiring a larger energy per unit area to separate the surfaces. TEM images before and after contact were compared and no material transfer was identified within the detection limits of the instrument (0.2 nm on the probe based on the TEM resolution and 1 nm on the diamond due to vibration of the indenter). Additionally, there was not more than a few atoms of material transfer in the simulated testing. Therefore, while the bond density appears to increase with applied load, the separation of the bodies still occurs at the original interface between the materials.

6.2.5 Conclusions

Using 77 compression-and-adhesion tests performed on well-controlled silicon-diamond interfaces inside a TEM and complementary atomistic simulations, we found that the strength of adhesion increases with applied stress. After systematically ruling out other explanations for varying work of adhesion, the increase is attributed to changes in atomic bonding across the interface. This effect causes a seven-fold increase in adhesion with externally applied stresses up to 11 GPa. In general, the findings reported here support newer models of contact, in which the work of adhesion is not represented as a static property of the interface, but instead as having a well-defined functional dependence on applied stress.

7.0 In-Process and Future Work

7.1 Understanding the Atomic-Scale Mechanisms Governing the Increase in Adhesion Strength with Applied Stress

7.1.1 *In situ* TEM and Matched Molecular Dynamics for Self-Mated TiO_2 Nanocontacts

The prior section demonstrated load-dependent adhesion in a silicon-carbon contact; the purpose of our ongoing work is to understand whether this behavior is unique to that material system or is exhibited by other covalently bonded materials. *In situ* TEM contact tests were conducted on a different material system of self-mated TiO_2 (anatase) to measure adhesive force as a function of maximum force. The experimental tests were conducted using a TiO_2 coated AFM probe that is brought into contact with a TiO_2 nanoparticle (Fig. 25a,b). The nanoparticles were drop-casted onto the silicon wedge, which was placed on the indenter. The applied and adhesive forces were measured using the methods described in Sect. 3.1. The matched molecular dynamics simulations were created for TiO_2 contacts using a ReaxFF potential [158] (Fig. 25c).

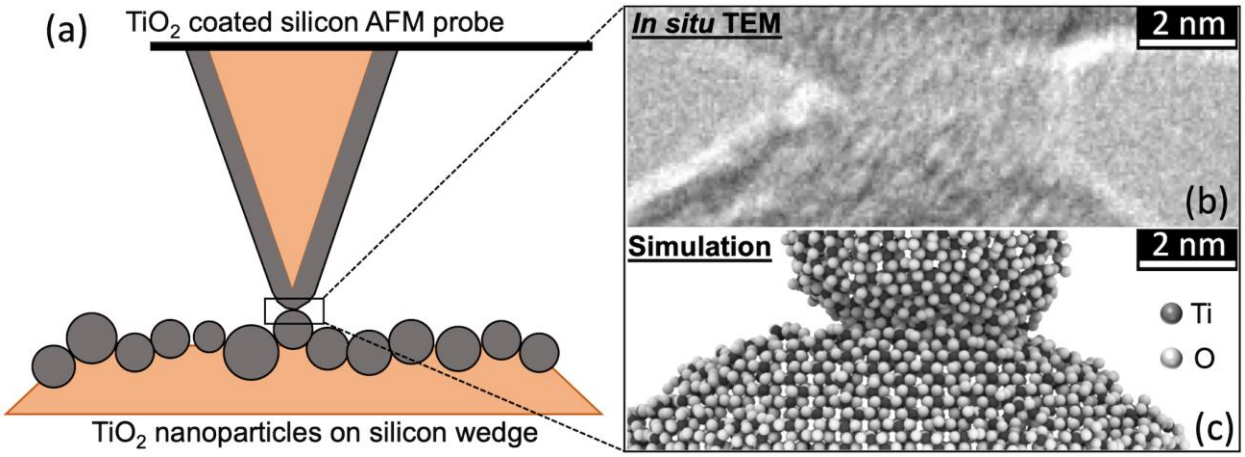

Figure 25. *In situ* TEM contact tests were conducted for self-mated contacts of TiO_2. The contact tests were performed by bringing a TiO_2 coated AFM probe into contact with a TiO_2 nanoparticle (a). The nanoscale contact was loaded to various maximum forces, and adhesive forces were measured for both the experiments (b) and atomistic simulations (c).

7.1.2 Increase in Work of Adhesion with Applied Stress for TiO_2 Nanocontacts

The effective modulus E_{eff} for TiO_2 contact is 124.0 GPa, calculated from the elastic modulus of TiO_2, E = 230 GPa and Poisson's ratio ν = 0.27. The effective radius R was measured by measuring the radius of TiO_2 coated AFM probe and nanoparticle before and after all tests from high-resolution TEM images. Using the measured adhesive force and effective radius, the work of adhesion is calculated using the Maugis-Dugdale model. The mean applied stress is calculated using the procedure descried in Sect. 6.2.2.

The work of adhesion as a function of applied stress for TiO_2 nanocontacts is shown in Fig. 26. The work of adhesion increases approximately from 0.5 J/m^2 at 2.5 GPa up to 7 J/m^2 at high stresses. The increase is gradual at low stresses where deformation is expected to be elastic

(until 4.5 GPa) and then increases rapidly at the higher stresses of elastic-plastic deformation. This trend is very similar to that observed for silicon-diamond nanocontacts and suggests that this behavior is not unique to silicon-diamond contacts. The increasing trend of the work of adhesion with applied stress for TiO_2 contacts provides evidence that this behavior may be generalizable to many covalently bonded materials. For this class of materials, the loading modifies the atomic-scale interactions, which causes an increase in the adhesion strength of the interface.

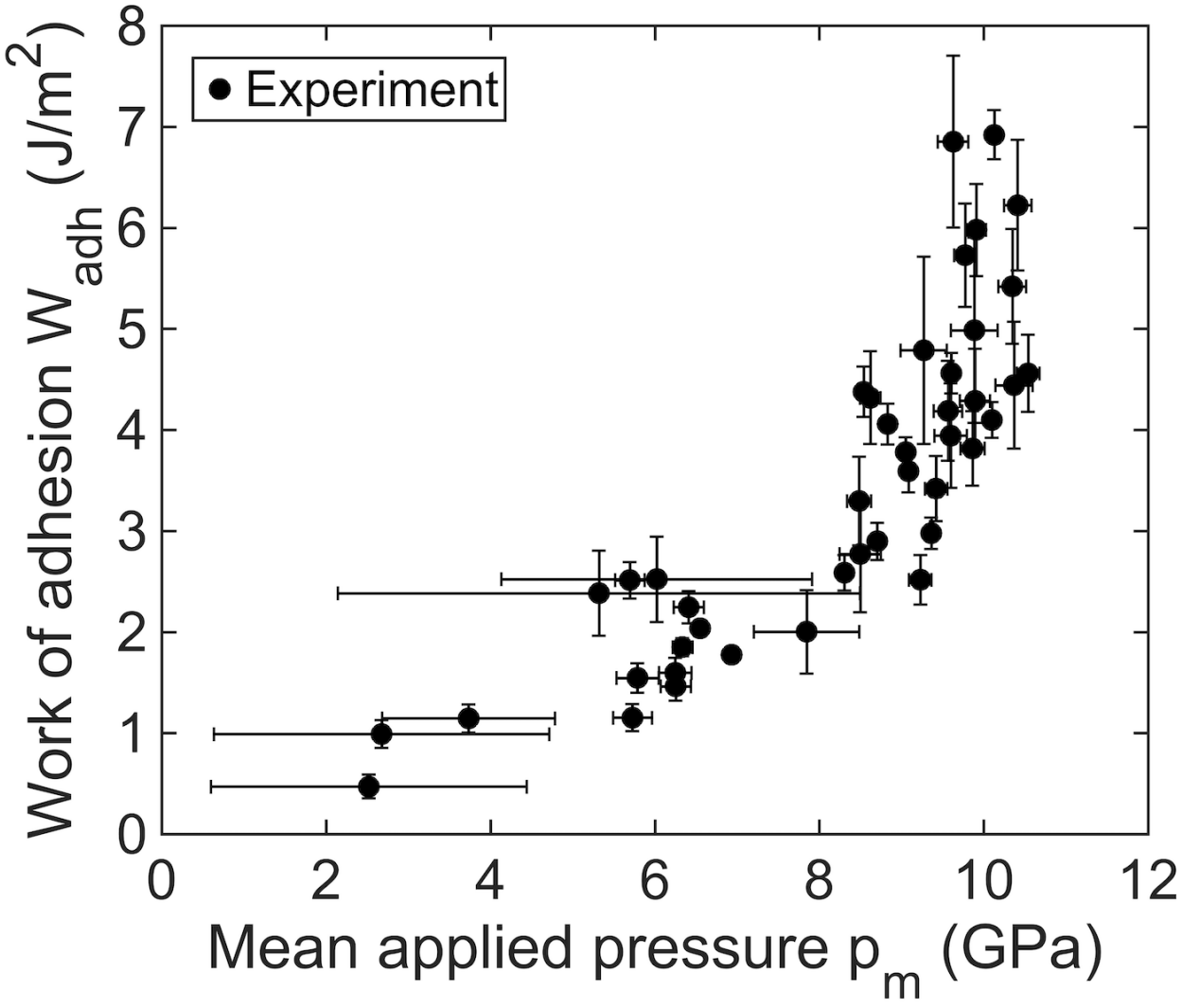

Figure 26. The work of adhesion increases with applied stress from TiO_2 nanocontacts. The increase is gradual at low stresses where the deformation is elastic (until 4.5 GPa) and then increases rapidly at the high stresses where the deformation is elastic-plastic.

7.1.3 Possible Origins of the Increase in Work of Adhesion with Stress for Nanoscale Contacts

After ruling out possible explanations for the increase in work of adhesion due to electron-beam induced reactions, shape change by inelastic deformation, and time-dependent deformation (see Sect. 6.2.4), the increase in work of adhesion is attributed to atomic-scale bonding at the interface. In previous work on the rate-and-state friction studies, the frictional strength is observed to increase with time (known as "contact aging") [167, 168], as well as with normal stress [169], and temperature [170]. In these studies, the increase in frictional strength is due to the increase in bond formation at the interface, which is known as "contact quality" [168, 170]. By contrast, the present results show no change in measured adhesion as a function of hold time (Fig. 24). Thus, the bond formation at the interface may depend only on the applied normal stress. The prediction of the "contact quality" hypothesis is that the increase in work of adhesion is due to the increase in bond density with the applied load. Another possible explanation for the increase in the work of adhesion could be due to the increase in true contact area, which could be possible due to local flattening of the atomic-scale roughness with the applied load (known as "contact quantity"). The prediction of the "contact quantity" hypothesis is that the increase in the work of adhesion is due to the increase in the true contact area. In continuum mechanics, such behavior is commonly known as "strength-limited pop-off" [171, 172], where the adhesive force scales linearly with contact area, and the bonds break uniformly across the interface.

Currently, work is ongoing to test different hypothesis discussed above to determine which atomic-scale mechanism is causing the increase in adhesion strength with applied stress for both the silicon-diamond and TiO_2 contacts.

8.0 Conclusions

The present dissertation studied contact behavior of nanoscale contacts using *in situ* TEM and matched molecular dynamics simulations. The *in situ* TEM setup enabled characterization of the geometry of the contact bodies with sub-nanometer resolution and direct real-time visualization of the contact interface as a function of applied and adhesive forces .The contact size was measured using three independent measurements: (i) direct measurements from *in situ* TEM video of the contact; (ii) direct measurements from the atomistic simulations that were performed for nanocontacts with precisely-matched materials, crystal orientations, geometry, and loading conditions; and (iii) measurements of conductance extracted from real-time current-voltage sweeps. In this final chapter, the most important results will be reviewed regarding the adhesion and contact size of the nanoscale contacts, and its impact on technological-relevant applications and the fundamental understanding of the contact behavior for different classes of materials.

For platinum noble-metal nanocontacts, it was observed that the direct measurements of the contact radius exceed the predictions of continuum contact mechanics by 40%–164%, depending on the continuum model applied. The physical mechanism for this deviation is found to be dislocation activity in the near-surface material, which is fully reversed upon unloading. The reversible dislocation behavior causes the softening of the contact−increases the size of the contact significantly than the elastic contact models. An empirical modification to the contact mechanics models is suggested which accurately predicts the contact size by using the effective elastic modulus equal to half of the true effective elastic modulus of the platinum nanocontact. The present finding provides a more accurate and complete understanding on the effect of the dislocation activity on the contact properties for noble metal contacts.

For the same nanocontacts, electron transport models under-predict the contact size by more than 95% to that of experiments and simulations. The low conductance of the platinum nanocontacts was due to a robust monolayer of surface species on the contact interface. The surface layer plays a significant role in the electrical transport of the platinum nanocontacts. The surface layer was observed to be resistant to loading, sliding, and wear of the probe. The relationship between contact size and current is predicted better with tunneling theory rather than the ballistic model. The present finding has critical implications for nanodevices and conductive AFM. In these applications, quantitative measurement and prediction of the current depends on the contact size, and the ballistic electrical transport model is frequently used. The present investigation demonstrates that an empirical model based on the tunneling theory can accurately determine the contact size from electrical transport measurements for platinum nanocontacts.

For silicon-diamond nanocontacts, the present investigation demonstrates two critical findings. First, from a single contact test using experiment and simulation, it was observed that the measured contact area as a function of force showed hysteretic behavior. The contact mechanics model could be accurately fit using a reasonable value of the effective elastic modulus for the unloading portion of the curve but could not fit the loading. The loading portion of the curve was fit with the same model but with varying work of adhesion with applied force. Second, using a combined total of 77 experiment and simulation tests, it was observed that the work of adhesion increases with applied stress. After ruling out the possible effects for varying adhesion—electron-beam induced reactions, shape change by inelastic deformation, and time-dependent deformation—the present results are attributed to the increase in adhesion strength due to the modifications of the atomic-scale interactions by the applied stress. For another covalently bonded

system of self-mated contacts of TiO_2 similar trend of increasing work of adhesion with applied stress was observed.

The broad implication of the increasing adhesion strength with applied stress is for the accurate modeling and prediction of adhesion for contacts. From a continuum modeling standpoint, the present results suggest an improvement in the descriptions of contacts that have been used widely used to describe adhesion, as well as mechanical and functional properties. These models assume that the work of adhesion between two materials is constant. The present findings imply that the work of adhesion is not a static property of the interface, but instead has a well-defined functional dependence on applied stress.

The present dissertation work contributes towards the fundamental understanding of the contact behavior for different material systems. There are two crucial implications of the present work. First, the contact mechanics models are insufficient to predict contact properties for real-world nanoscale structures, and modifications are suggested to account for the atomic-scale phenomenon. Second, different physical mechanisms govern the contact properties such as contact size, deformation, and adhesion for metals and covalent solids.

Bibliography

1. Chou, S.Y., Krauss, P.R., Renstrom, P.J.: Imprint of sub-25 nm vias and trenches in polymers. Appl. Phys. Lett. 67, 3114–3116 (1995).

2. Piner, R.D., Zhu, J., Xu, F., Hong, S., Mirkin, C.A.: "Dip-pen" nanolithography. Science. 283, 661–663 (1999).

3. Brown, B.P., Picco, L., Miles, M.J., Faul, C.F.J.: Conductive-AFM patterning of organic semiconductors. Small. 11, 5054–5058 (2015).

4. Kim, T.-H., Chung, D.-Y., Ku, J., Song, I., Sul, S., Kim, D.-H., Cho, K.-S., Choi, B.L., Kim, J.M., Hwang, S., Kim, K.: Heterogeneous stacking of nanodot monolayers by dry pick-and-place transfer and its applications in quantum dot light-emitting diodes. Nat. Commun. 4, 2637 (2013).

5. Park, J.Y., Maier, S., Hendriksen, B., Salmeron, M.: Sensing current and forces with SPM. Mater. Today. 13, 38–45 (2010).

6. Jesse, S., Balke, N., Eliseev, E., Tselev, A., Dudney, N.J., Morozovska, A.N., Kalinin, S. V: Direct mapping of ionic transport in a si anode on the nanoscale: time domain electrochemical strain spectroscopy study. ACS Nano. 5, 9682–9695 (2011).

7. Ou, X., Kanungo, P. Das, Kögler, R., Werner, P., Gösele, U., Skorupa, W., Wang, X.: Carrier profiling of individual Si nanowires by scanning spreading resistance microscopy. Nano Lett. 10, 171–175 (2010).

8. Eyben, P., Denis, S., Clarysse, T., Vandervorst, W.: Progress towards a physical contact model for scanning spreading resistance microscopy. Mater. Sci. Eng. B. 102, 132–137 (2003).

9. Bussmann, E., Rudolph, M., Subramania, G.S., Misra, S., Carr, S.M., Langlois, E., Dominguez, J., Pluym, T., Lilly, M.P., Carroll, M.S.: Scanning capacitance microscopy registration of buried atomic-precision donor devices. Nanotechnology. 26, 085701 (2015).

10. Sadat, S., Tan, A., Chua, Y.J., Reddy, P.: Nanoscale thermometry using point contact thermocouples. Nano Lett. 10, 2613–2617 (2010).

11. Loh, O.Y., Espinosa, H.D.: Nanoelectromechanical contact switches. Nat. Nanotechnol. 7, 283–295 (2012).

12. Rebeiz, G.M., Muldavin, J.B.: RF MEMS switches and switch circuits. IEEE Microw. Mag. 2, 59–71 (2001).

13. Hertz, H.: On the contact of elastic solids. J. reine angew. Math. 92, 156–171 (1881).

14. Israelachvili, J.N.: Intermolecular and surface forces: Revised third edition. Academic press (2011).

15. Bradley, R.S.R.: The cohesive force between solid surfaces and the surface energy of solids. London, Edinburgh, Dublin Philos. Mag. J. Sci. 13, 853–862 (1932).

16. Derjaguin, B. V, Muller, V.M., Toporov, Y.U.P.: Effect of contact deformation on the adhesion of particles. J. Colloid Interface Sci. 52, 105–108 (1975).

17. Johnson, K.L., Kendall, K., Roberts, A.D.: Surface energy and the contact of elastic solids. Proc. R. Soc. London A Math. Phys. Eng. Sci. 324, 301–313 (1971).

18. Tabor, D.: Surface forces and surface interactions. J. Colloid Interface Sci. 58, 2–13 (1977).

19. Maugis, D.: Adhesion of spheres: The JKR-DMT transition using a dugdale model. J. Colloid Interface Sci. 150, 243–269 (1992).

20. Carpick, R.W., Ogletree, D.F., Salmeron, M.: A general equation for fitting contact area and friction vs load measurements, J. Colloid Interface Sci. 211, 395–400 (1999).

21. Piétrement, O., Troyon, M.: General equations describing elastic indentation depth and normal contact stiffness versus load. J. Colloid Interface Sci. 226, 166–171 (2000).

22. Grierson, D.S., Flater, E.E., Carpick, R.W.: Accounting for the JKR-DMT transition in adhesion and friction measurements with atomic force microscopy. J. Adhes. Sci. Technol. 19, 291–311 (2005).

23. Grierson, D.S., Liu, J., Carpick, R.W., Turner, K.T.: Adhesion of nanoscale asperities with power-law profiles. J. Mech. Phys. Solids. 61, 597–610 (2013).

24. Zheng, Z., Yu, J.: Using the Dugdale approximation to match a specific interaction in the adhesive contact of elastic objects. J. Colloid Interface Sci. 310, 27–34 (2007).

25. Carpick, R.W., Agrait, N., Ogletree, D.F., Salmeron, M.: Measurement of interfacial shear (friction) with an ultrahigh vacuum atomic force microscope. J. Vac. Sci. Technol. B Microelectron. Nanom. Struct. 14, 1289 (1996).

26. Popov, V.L.: Contact mechanics and friction. Springer (2010).

27. Lantz, M.A., O'Shea, S.J., Welland, M.E.: Simultaneous force and conduction measurements in atomic force microscopy. Phys. Rev. B. 56, 15345 (1997).

28. Enachescu, M., van den Oetelaar, R.J.A., Carpick, R.W., Ogletree, D.F., Flipse, C.F.J., Salmeron, M.: Observation of proportionality between friction and contact area at the nanometer scale. Tribol. Lett. 7, 73 (1999).

29. Sharvin, Y. V: A possible method for studying fermi surfaces. Sov. Phys. JETP-USSR. 21, 655–656 (1965).

30. Enachescu, M., van den Oetelaar, R.J.A., Carpick, R.W., Ogletree, D.F., Flipse, C.F.J., Salmeron, M.: Atomic force microscopy study of an ideally hard contact: The diamond(111) tungsten carbide interface. Phys. Rev. Lett. 81, 1877–1880 (1998).

31. Lessel, M., Loskill, P., Hausen, F., Gosvami, N.N., Bennewitz, R., Jacobs, K.: Impact of van der waals interactions on single asperity friction. Phys. Rev. Lett. 111, 035502 (2013).

32. Bernal, R.A., Chen, P., Schall, J.D., Harrison, J.A., Jeng, Y.R., Carpick, R.W.: Influence of chemical bonding on the variability of diamond-like carbon nanoscale adhesion. Carbon N. Y. 128, 267–276 (2018).

33. Piétrement, O., Troyon, M.: Study of the interfacial shear strength pressure dependence by modulated lateral force microscopy. Langmuir. 17, 6540–6546 (2001).

34. Gao, J., Luedtke, W.D., Israelachvili, J.N., Ruths, M., Gourdon, D., Landman, U.: Frictional Forces and Amontons' Law: From the Molecular to the Macroscopic Scale. J. Phys. Chem. B. 108, 3410–3425 (2004).

35. Socoliuc, A., Bennewitz, R., Gnecco, E., Meyer, E.: Transition from stick-slip to continuous sliding in atomic friction: entering a new regime of ultralow friction. Phys. Rev. Lett. 92, 134301 (2004).

36. Dong, Y., Li, Q., Martini, A.: Molecular dynamics simulation of atomic friction: a review and guide. J. Vac. Sci. Technol. A. 31, 30801 (2013).

37. Chandross, M., Lorenz, C.D., Stevens, M.J., Grest, G.S.: Simulations of nanotribology with realistic probe tip models. Langmuir. 24, 1240–1246 (2008).

38. Brukman, M.J., Gao, G., Nemanich, R.J., Harrison, J.A.: Temperature dependence of single-asperity diamond-diamond friction elucidated using AFM and MD simulations. J. Phys. Chem. C. 112, 9358–9369 (2008).

39. Li, Q., Dong, Y., Perez, D., Martini, A., Carpick, R.W.: Speed dependence of atomic stick-slip friction in optimally matched experiments and molecular dynamics simulations. Phys. Rev. Lett. 106, 126101 (2011).

40. Vahdat, V., Ryan, K.E., Keating, P.L., Jiang, Y., Adiga, S.P., Schall, J.D., Turner, K.T., Harrison, J.A., Carpick, R.W.: Atomic-scale wear of amorphous hydrogenated carbon during intermittent contact: a combined study using experiment, simulation, and theory. ACS Nano. 8, 7027–7040 (2014).

41. Mo, Y., Szlufarska, I.: Roughness picture of friction in dry nanoscale contacts. Phys. Rev. B. 81, 035405 (2010).

42. Reedy, E.D.: Thin-coating contact mechanics with adhesion. J. Mater. Res. 21, 2660–2668 (2006).

43. Luan, B., Robbins, M.O.: The breakdown of continuum models for mechanical contacts. Nature. 435, 929–932 (2005).

44. Luan, B., Robbins, M.O.: Contact of single asperities with varying adhesion: Comparing continuum mechanics to atomistic simulations. Phys. Rev. E. 74, 26111 (2006).

45. Cha, P.-R., Srolovitz, D.J., Kyle Vanderlick, T.: Molecular dynamics simulation of single asperity contact. Acta Mater. 52, 3983–3996 (2004).

46. Szlufarska, I., Chandross, M., Carpick, R.W.: Recent advances in single-asperity nanotribology. J. Phys. D. Appl. Phys. 41, 123001 (2008).

47. Ryan, K.E., Keating, P.L., Jacobs, T.D.B., Grierson, D.S., Turner, K.T., Carpick, R.W., Harrison, J.A.: Simulated adhesion between realistic hydrocarbon materials: effects of composition, roughness, and contact point. Langmuir. 30, 2028–2037 (2014).

48. Mo, Y., Turner, K.T., Szlufarska, I.: Friction laws at the nanoscale. Nature. 457, 1116–1119 (2009).

49. Solhjoo, S., Vakis, A.I.: Definition and detection of contact in atomistic simulations. Comput. Mater. Sci. 109, 172–182 (2015).

50. Kiener, D., Motz, C., Schöbert, T., Jenko, M., Dehm, G.: Determination of mechanical properties of copper at the micron scale. Adv. Eng. Mater. 8, 1119–1125(2006).

51. Ng, K.S., Ngan, A.H.W.: Stochastic nature of plasticity of aluminum micro-pillars. Acta Mater. 56, 1712–1720 (2008).

52. Greer, J.R., Nix, W.D.: Nanoscale gold pillars strengthened through dislocation starvation. Phys. Rev. B - Condens. Matter Mater. Phys. 73, 245410 (2006).

53. Shan, Z.W., Mishra, R.K., Syed Asif, S.A., Warren, O.L., Minor, A.M.: Mechanical annealing and source-limited deformation in submicrometre- diameter Nicrystals. Nat. Mater. 7, 115–119 (2008).

54. Kim, J.Y., Greer, J.R.: Size-dependent mechanical properties of molybdenum nanopillars. Appl. Phys. Lett. 93, 101916 (2008).

55. Uchic, M.D., Shade, P.A., Dimiduk, D.M.: Plasticity of Micrometer-Scale Single Crystals in Compression. Annu. Rev. Mater. Res. 39, 361–386 (2009).

56. Asenjo, A., Jaafar, M., Carrasco, E., Rojo, J.M.: Dislocation mechanisms in the first stage of plasticity of nanoindented Au(111) surfaces. Phys. Rev. B - Condens. Matter Mater. Phys. 73, 075431 (2006).

57. Filleter, T., Bennewitz, R.: Nanometre-scale plasticity of Cu(100). Nanotechnology. 18, 044004 (2007).

58. Kraft, O., Gruber, P.A., Mönig, R., Weygand, D.: Plasticity in Confined Dimensions. Annu. Rev. Mater. Res. 40, 293–317 (2010).

59. Merkle, A.P., Marks, L.D.: Liquid-like tribology of gold studied by in situ TEM. Wear. 265, 1864–1869 (2008).

60. Zheng, H., Cao, A., Weinberger, C.R., Huang, J.Y., Du, K., Wang, J., Ma, Y., Xia, Y., Mao, S.X.: Discrete plasticity in sub-10-nm-sized gold crystals. Nat. Commun. 1, 144 (2010).

61. Sun, J., He, L., Lo, Y.-C., Xu, T., Bi, H., Sun, L., Zhang, Z., Mao, S.X., Li, J.: Liquid-like pseudoelasticity of sub-10-nm crystalline silver particles. Nat. Mater. 13, 1007–1012 (2014).

62. Zhong, L., Sansoz, F., He, Y., Wang, C., Zhang, Z., Mao, S.X.: Slip-activated surface creep with room-temperature super-elongation in metallic nanocrystals. Nat. Mater. 16, 439 (2016).

63. Agraït, N.: Quantum properties of atomic-sized conductors. Phys. Rep. 377, 81–279 (2003).

64. Masuda, H., Kizuka, T.: Structure, electrical, and mechanical properties of silver nanocontacts. Jpn. J. Appl. Phys. 49, 45202 (2010).

65. Rodrigues, V., Ugarte, D.: Metal nanowires: atomic arrangement and electrical transport properties. Nanotechnology. 13, 404 (2002).

66. Kizuka, T.: Atomic process of point contact in gold studied by time-resolved high-resolution transmission electron microscopy. Phys. Rev. Lett. 81, 4448 (1998).

67. Lu, Y., Huang, J.Y., Wang, C., Sun, S., Lou, J.: Cold welding of ultrathin gold nanowires. Nat. Nanotechnol. 5, 218–224 (2010).

68. Pereira, Z.S., da Silva, E.Z.: Cold welding of gold and silver nanowires: a molecular dynamics study. J. Phys. Chem. C. 115, 22870–22876 (2011).

69. Cross, G.L.W., Schirmeisen, A., Grütter, P., Dürig, U.T.: Plasticity, healing and shakedown in sharp-asperity nanoindentation. Nat. Mater. 5, 370–376 (2006).

70. Petzold, C., Koch, M., Bennewitz, R.: Friction force microscopy of tribochemistry and interfacial ageing for the SiOx/Si/Au system. Beilstein J. Nanotechnol. 9, 1647–1658(2018).

71. Gosvami, N.N., Filleter, T., Egberts, P., Bennewitz, R.: Microscopic Friction Studies on Metal Surfaces. Tribol. Lett. 39, 19–24 (2010).

72. Bennewitz, R., Hausen, F., Gosvami, N.N.: Nanotribology of clean and modified gold surfaces. J. Mater. Res. 28, 1279–1288 (2013).

73. Bennewitz, R., Gyalog, T., Guggisberg, M., Bammerlin, M., Meyer, E., Güntherodt, H.J.: Atomic-scale stick-slip processes on Cu(111). Phys. Rev. B - Condens. Matter Mater. Phys. 60, R11301 (1999).

74. Caron, A., Louzguine-Luzguin, D. V., Bennewitz, R.: Structure vs chemistry: Friction and wear of Pt-based metallic surfaces. ACS Appl. Mater. Interfaces. 5, 11341–11347 (2013).

75. Slade, P.G.: Electrical contacts. Boca Raton, FL: CRC Press (2013).

76. Philip, B.F., David, T., Ingram, T.G.: The area of contact between stationary and moving surfaces. Proc. R. Soc. London. Ser. A. Math. Phys. Sci. 169, 391–413 (1939).

77. Wexler, G.: The size effect and the non-local Boltzmann transport equation in orifice and disk geometry. Proc. Phys. Soc. 89, 927 (1966).

78. Nikolić, B., Allen, P.B.: Electron transport through a circular constriction. Phys. Rev. B. 60, 3963 (1999).

79. Eckmann, A., Felten, A., Mishchenko, A., Britnell, L., Krupke, R., Novoselov, K.S., Casiraghi, C.: Probing the nature of defects in graphene by Raman spectroscopy. Nano Lett. 12, 3925–3930 (2012).

80. Celano, U., Hantschel, T., Giammaria, G., Chintala, R.C., Conard, T., Bender, H., Vandervorst, W.: Evaluation of the electrical contact area in contact-mode scanning probe microscopy. J. Appl. Phys. 117, 214305 (2015).

81. Hu, X., Lee, J., Berman, D., Martini, A.: Substrate effect on electrical conductance at a nanoasperity-graphene contact. Carbon N. Y. 137, 118–124 (2018).

82. Toler, B.F., Coutu Jr, R.A., McBride, J.W.: A review of micro-contact physics for microelectromechanical systems (MEMS) metal contact switches. J. Micromechanics Microengineering. 23, 103001 (2013).

83. Li, L., Song, W., Zhang, G., Jia, D.: An electrical contact resistance model including roughness effect for a rough MEMS switch. J. Micromechanics Microengineering. 22, 115023 (2012).

84. Jensen, B.D., Huang, K., Chow, L.L.W., Kurabayashi, K.: Low-force contact heating and softening using micromechanical switches in diffusive-ballistic electron-transport transition. Appl. Phys. Lett. 86, 023507 (2005).

85. Rezvanian, O., Zikry, M.A., Brown, C., Krim, J.: Surface roughness, asperity contact and gold RF MEMS switch behavior. J. Micromechanics Microengineering. 17, 2006–2015 (2007).

86. Majumder, S., McGruer, N.E., Adams, G.G., Zavracky, P.M., Morrison, R.H., Krim, J.: Study of contacts in an electrostatically actuated microswitch. Sensors Actuators, A Phys. 93, 19–26 (2001).

87. Brown, C., Rezvanian, O., Zikry, M.A., Krim, J.: Temperature dependence of asperity contact and contact resistance in gold RF MEMS switches. J. Micromechanics Microengineering. 19, 025006 (2009).

88. Kogut, L., Komvopoulos, K.: Electrical contact resistance theory for conductive rough surfaces. J. Appl. Phys. 94, 3153–3162 (2003).

89. Kogut, L., Komvopoulos, K.: Electrical contact resistance theory for conductive rough surfaces separated by a thin insulating film. J. Appl. Phys. 95, 576–585 (2004).

90. Coutu, R.A., Reid, J.R., Cortez, R., Strawser, R.E., Kladitis, P.E.: Microswitches with sputtered Au, AuPd, Au-on-AuPt, and AuPtCu alloy electric contacts. IEEE Trans. Components Packag. Technol. 29, 341–349 (2006).

91. Zhou, Z., Nie, W., Xi, Z., Wang, X.: Electrical contact performance of MEMS acceleration switch fabricated by UV-LIGA technology. Microsyst. Technol. 21, 2271–2278 (2015).

92. Valencia, D., Wilson, E., Jiang, Z., Valencia-Zapata, G.A., Wang, K.C., Klimeck, G., Povolotskyi, M.: Grain-Boundary resistance in copper interconnects: from an atomistic model to a neural network. Phys. Rev. Appl. 9, 044005 (2018).

93. Wang, J., Wu, Z., Mao, C., Zhao, Y., Yang, J., Chen, Y.: Effect of electrical contact resistance on measurement of thermal conductivity and wiedemann-franz law for individual metallic nanowires. Sci. Rep. 8, 4862 (2018).

94. Erts, D., Olin, H., Ryen, L., Olsson, E., Tholen, A.: Maxwell and Sharvin conductance in gold point contacts investigated using TEM-STM. Phys. Rev. B. 61, 12725–12727 (2000).

95. Oliver, D.J., Maassen, J., El Ouali, M., Paul, W., Hagedorn, T., Miyahara, Y., Qi, Y., Guo, H., Grütter, P.: Conductivity of an atomically defined metallic interface. Proc. Natl. Acad. Sci. U. S. A. 109, 19097–19102 (2012).

96. Streller, F., Wabiszewski, G.E., Carpick, R.W.: Development and Assessment of Next-Generation Nanoelectromechanical Switch Contact Materials. 14th International conference on nanotechnology, Toronto, ON, pp. 141–145 (2014).

97. Yang, F., Carpick, R.W., Srolovitz, D.J.: Mechanisms of contact, adhesion, and failure of metallic nanoasperities in the presence of adsorbates: toward conductive contact design. ACS Nano. 11, 490–500 (2016).

98. Qi, Y., Yang, J., Rappe, A.M.: Theoretical modeling of tribochemical reaction on Pt and Au contacts: mechanical load and catalysis. ACS Appl. Mater. Interfaces. 8, 7529–7535 (2016).

99. Jacobs, T.D.B., Martini, A.: Measuring and understanding contact area at the nanoscale: a review. Appl. Mech. Rev. 69, 60802–60818 (2017).

100. Jacobs, T.D.B., Lefever, J.A., Carpick, R.W.: Measurement of the length and strength of adhesive interactions in a nanoscale silicon–diamond interface. Adv. Mater. Interfaces. 2, 1400547 (2015).

101. Vishnubhotla, S.B., Chen, R., Khanal, S.R., Hu, X., Martini, A., Jacobs, T.D.B.: Matching atomistic simulations and in situ experiments to investigate the mechanics of nanoscale contact. Tribol. Lett. 67, 97 (2019).

102. Williams, D.B., Carter, C.B.: The transmission electron microscope. Springer (1996).

103. Sader, J.E., Chon, J.W.M., Mulvaney, P.: Calibration of rectangular atomic force microscope cantilevers. Rev. Sci. Instrum. 70, 3967–3969 (1999).

104. Chen, R., Vishnubhotla, S.B., Khanal, S.R., Jacobs, T.D.B., Martini, A.: Quantifying the pressure-dependence of work of adhesion in silicon-diamond contacts. Appl. Phys. Lett. 116, 051602 (2020).

105. Vishnubhotla, S.B., Chen, R., Khanal, S.R., Li, J., Stach, E.A., Martini, A., Jacobs, T.D.B.: Quantitative measurement of contact area and electron transport across platinum nanocontacts for scanning probe microscopy and electrical nanodevices. Nanotechnology. 30, 45705 (2019).

106. Vishnubhotla, S.B., Chen, R., Khanal, S.R., Martini, A., Jacobs, T.D.B.: Understanding contact between platinum nanocontacts at low loads: the effect of reversible plasticity. Nanotechnology. 30, 035704 (2019).

107. Jacobs, T.D.B., Ryan, K.E., Keating, P.L., Grierson, D.S., Lefever, J.A., Turner, K.T., Harrison, J.A., Carpick, R.W.: The effect of atomic-scale roughness on the adhesion of nanoscale asperities: a combined simulation and experimental investigation. Tribol. Lett. 50, 81–93 (2013).

108. Jacobs, T.D.B., Carpick, R.W.: Nanoscale wear as a stress-assisted chemical reaction. Nat. Nanotechnol. 8, 108–112 (2013).

109. Liu, J., Notbohm, J.K., Carpick, R.W., Turner, K.T.: Method for characterizing nanoscale wear of atomic force microscope tips. ACS Nano. 4, 3763–3772 (2010).

110. Johnson, K.L.: Contact mechanics. Cambridge University Press (1987).

111. Jiang, Y., Harrison, J.A., Schall, J.D., Ryan, K.E., Carpick, R.W., Turner, K.T.: Correcting for tip geometry effects in molecular simulations of single-asperity contact. Tribol. Lett. 65, 78 (2017).

112. Plimpton, S.: Fast parallel algorithms for short-range molecular dynamics. J. Comput. Phys. 117, 1–19 (1995).

113. Foiles, S.M., Baskes, M.I., Daw, M.S.: Embedded-atom-method functions for the FCC metals Cu, Ag, Au, Ni, Pd, Pt, and their alloys. Phys. Rev. B. 33, 7983–7991 (1986).

114. Liem, S.Y., Chan, K.Y.: Effective pairwise potential for simulations of adsorbed platinum. Mol. Phys. 86, 939–949 (1995).

115. Merker, J., Lupton, D., Töpfer, M., Knake, H.: High temperature mechanical properties of the platinum group metals. Platin. Met. Rev. 45, 74–82 (2001).

116. Oliver, W.C., Pharr, G.M.: Measurement of hardness and elastic modulus by instrumented indentation: Advances in understanding and refinements to methodology. J. Mater. Res. 19, 3–20 (2004).

117. Stroh, A.N.: Force on a moving dislocation. Phys. Rev. 128, 55–61 (1962).

118. Kogut, L., Etsion, I.: Elastic-plastic contact analysis of a sphere and a rigid flat. J. Appl. Mech. 69, 657 (2002).

119. Oliver, W.C., Pharr, G.M.: An improved technique for determining hardness and elastic-modulus using load and displacement sensing indentation experiments. J. Mater. Res. 7, 1564–1583 (1992).

120. Greer, J.R., Kim, J.Y., Burek, M.J.: The in-situ mechanical testing of nanoscale single-crystalline nanopillars, JOM. 61, 19 (2009).

121. Sneddon, I.N.: The relation between load and penetration in the axisymmetric boussinesq problem for a punch of arbitrary profile. Int. J. Eng. Sci. 3, 47–57 (1965).

122. Kiely, J.D., Hwang, R.Q., Houston, J.E.: Effect of surface steps on the plastic threshold in nanoindentation. Phys. Rev. Lett. 81, 4424–4427 (1998).

123. Kelchner, C.L., Plimpton, S.J., Hamilton, J.C.: Dislocation nucleation and defect structure during surface indentation. Phys. Rev. B. 58, 11085–11088 (1998).

124. Zimmerman, J.A., Kelchner, C.L., Klein, P.A., Hamilton, J.C., Foiles, S.M.: Surface step effects on nanoindentation. Phys. Rev. Lett. 87, 165507 (2001).

125. Kittel, C.: Introduction to solid state physics. Wiley (1916).

126. Ashcroft, N.W., Mermin, N.D.: Solid State Physics. Holt, Rinehart and Winston, New York (1976).

127. Dye, D.H., Ketterson, J.B., Crabtree, G.W.: The Fermi surface of platinum. J. Low Temp. Phys. 30, 813–838 (1978).

128. Mayadas, A.F., Shatzkes, M.: Electrical-resistivity model for polycrystalline films: The case of arbitrary reflection at external surfaces. Phys. Rev. B. 1, 1382–1389 (1970).

129. Argibay, N., Mogonye, J.E., Michael, J.R., Goeke, R.S., Kotula, P.G., Scharf, T.W., Dugger, M.T., Prasad, S. V.: On the thermal stability of physical vapor deposited oxide-hardened nanocrystalline gold thin films. J. Appl. Phys. 117, 145302 (2015).

130. Gotsmann, B., Lantz, M.A.: Quantized thermal transport across contacts of rough surfaces. Nat. Mater. 12, 59–65 (2013).

131. Cheng, S., Robbins, M.O.: Defining contact at the atomic scale. Tribol. Lett. 39, 329–348 (2010).

132. Pastewka, L., Robbins, M.O.: Contact area of rough spheres: large scale simulations and simple scaling laws. Appl. Phys. Lett. 108, 221601 (2016).

133. Rodrigues, V., Fuhrer, T., Ugarte, D.: Signature of atomic structure in the quantum conductance of gold nanowires. Phys. Rev. Lett. 85, 4124 (2000).

134. Krans, J.M., Muller, C.J., Yanson, I.K., Govaert, T.C.M., Hesper, R., van Ruitenbeek, J.M.: One-atom point contacts. Phys. Rev. B. 48, 14721 (1993).

135. Smit, R.H.M., Untiedt, C., Yanson, A.I., van Ruitenbeek, J.M.: Common origin for surface reconstruction and the formation of chains of metal atoms. Phys. Rev. Lett. 87, 266102 (2001).

136. Makk, P., Balogh, Z., Csonka, S., Halbritter, A.: Pulling platinum atomic chains by carbon monoxide molecules. Nanoscale. 4, 4739–4745 (2012).

137. Yanson, A.I., Bollinger, G.R., van den Brom, H.E., Agraït, N., van Ruitenbeek, J.M.: Formation and manipulation of a metallic wire of single gold atoms. Nat. 395, 783 (1998).

138. Ohnishi, H., Kondo, Y., Takayanagi, K.: Quantized conductance through individual rows of suspended gold atoms. Nature. 395, 780–783 (1998).

139. Simmons, J.G.: Generalized formula for the electric tunnel effect between similar electrodes separated by a thin insulating film. J. Appl. Phys. 34, 1793–1803 (1963).

140. Yoshida, H., Omote, H., Takeda, S.: Oxidation and reduction processes of platinum nanoparticles observed at the atomic scale by environmental transmission electron microscopy. Nanoscale. 6, 13113–13118 (2014).

141. Lantz, M.A., O'Shea, S.J., Welland, M.E.: Characterization of tips for conducting atomic force microscopy in ultrahigh vacuum. Rev. Sci. Instrum. 69, 1757 (1998).

142. Kumagai, T., Izumi, S., Hara, S., Sakai, S.: Development of bond-order potentials that can reproduce the elastic constants and melting point of silicon for classical molecular dynamics simulation. Comput. Mater. Sci. 39, 457–464 (2007).

143. Guo, Q., Izumisawa, S., Phillips, D.M., Jhon, M.S.: Surface morphology and molecular conformation for ultrathin lubricant films with functional end groups. J. Appl. Phys. 93, 8707–8709 (2003).

144. Yi, T., Ramasamy, U.S., Lichter, S., Martini, A.: Stability and structure of nanometer-thin perfluoropolyether films using molecular simulations. Tribol. Lett. 54, 119–127 (2014).

145. Huheey, T.L.: Cottrell, The strengths of chemical bonds. Butterworth, London (1958).

146. McSkimin, H.J., Andreatch Jr, P.: Elastic moduli of diamond as a function of pressure and temperature. J. Appl. Phys. 43, 2944–2948 (1972).

147. Hopcroft, M.A., Nix, W.D., Kenny, T.W.: What is the young's modulus of silicon? J. Microelectromechanical Syst. 19, 229–238 (2010).

148. Katainen, J., Paajanen, M., Ahtola, E., Pore, V., Lahtinen, J.: Adhesion as an interplay between particle size and surface roughness. J. Colloid Interface Sci. 304, 524–529 (2006).

149. Liu, D.L., Martin, J., Burnham, N.A.: Optimal roughness for minimal adhesion. Appl. Phys. Lett. 91, 043107 (2007).

150. Moore, N.W., Houston, J.E.: The pull-off force and the work of adhesion: new challenges at the nanoscale. J. Adhes. Sci. Technol. 24, 2531–2544 (2012).

151. Sumant, A. V, Grierson, D.S., Gerbi, J.E., Birrell, J., Lanke, U.D., Auciello, O., Carlisle, J.A., Carpick, R.W.: Toward the ultimate tribological interface: surface chemistry and nanotribology of ultrananocrystalline diamond. Adv. Mater. 17, 1039–1045 (2005).

152. Sumant, A. V., Grierson, D.S., Gerbi, J.E., Carlisle, J.A., Auciello, O., Carpick, R.W.: Surface chemistry and bonding configuration of ultrananocrystalline diamond surfaces and their effects on nanotribological properties. Phys. Rev. B. 76, 235429 (2007).

153. Milne, Z.B., Schall, J.D., Jacobs, T.D.B., Harrison, J.A., Carpick, R.W.: Covalent bonding and atomic-level plasticity increase adhesion in silicon-diamond nanocontacts. ACS Appl. Mater. Interfaces. 11, 40734–40748 (2019).

154. de Boer, M.P., Knapp, J.A., Michalske, T.A., Srinivasan, U., Maboudian, R.: Adhesion hysteresis of silane coated microcantilevers. Acta Mater. 48, 4531–4541 (2000).

155. Attard, P.: Interaction and deformation of viscoelastic particles: nonadhesive particles. Phys. Rev. E. 63, 61604 (2001).

156. Chen, Y.L., Helm, C.A., Israelachvili, J.N.: Molecular mechanisms associated with adhesion and contact angle hysteresis of monolayer surfaces. J. Phys. Chem. 95, 10736–10747 (1991).

157. Horn, R.G., Israelachvili, J.N., Pribac, F.: Measurement of the deformation and adhesion of solids in contact. J. Colloid Interface Sci. 115, 480–492 (1987).

158. Yeon, J., Van Duin, A.C.T.: ReaxFF molecular dynamics simulations of hydroxylation kinetics for amorphous and nano-silica structure, and its relations with atomic strain energy. J. Phys. Chem. C. 120, 305–317 (2016).

159. Yeon, J., van Duin, A.C.T., Kim, S.H.: Effects of water on tribochemical wear of silicon oxide interface: molecular dynamics (MD) study with reactive force field (ReaxFF). Langmuir. 32, 1018–1026 (2016).

160. Liu, D.L., Martin, J., Burnham, N.A.: Optimal roughness for minimal adhesion. Appl. Phys. Lett. 91, 43107 (2007).

161. Vandeperre, L.J., Giuliani, F., Lloyd, S.J., Clegg, W.J.: The hardness of silicon and germanium. Acta Mater. 55, 6307–6315 (2007).

162. Johnson, K.L., Keer, L.M.: Contact Mechanics. J. Tribol. 108, 659 (1986).

163. Bernal, R.A., Chen, P., Schall, J.D., Harrison, J.A., Jeng, Y.-R., Carpick, R.W.: Influence of chemical bonding on the variability of diamond-like carbon nanoscale adhesion. Carbon N. Y. 128, 267–276 (2018).

164. Piotrowski, P.L., Cannara, R.J., Gao, G., Urban, J.J., Carpick, R.W., Harrison, J.A.: Atomistic factors governing adhesion between diamond, amorphous carbon and model diamond nanocomposite surfaces. J. Adhes. Sci. Technol. 24, 2471–2498 (2010).

165. Zheng, K., Wang, C., Cheng, Y.-Q., Yue, Y., Han, X., Zhang, Z., Shan, Z., Mao, S.X., Ye, M., Yin, Y., Ma, E.: Electron-beam-assisted superplastic shaping of nanoscale amorphous silica. Nat. Commun. 1, 24 (2010).

166. Jacobs, T.D.B., Wabiszewski, G.E., Goodman, A.J., Carpick, R.W.: Characterizing nanoscale scanning probes using electron microscopy: a novel fixture and a practical guide. Rev. Sci. Instrum. 87, 13703 (2016).

167. Tian, K., Li, Z., Liu, Y., Gosvami, N.N., Goldsby, D.L., Szlufarska, I., Carpick, R.W.: Linear aging behavior at short timescales in nanoscale contacts. Phys. Rev. Lett. 124, 026801 (2020).

168. Li, Q., Tullis, T.E., Goldsby, D., Carpick, R.W.: Frictional ageing from interfacial bonding and the origins of rate and state friction. Nature. 480, 233–236 (2011).

169. Li, A., Liu, Y., Szlufarska, I.: Effects of interfacial bonding on friction and wear at silica/silica interfaces. Tribol. Lett. 56, 481–490 (2014).

170. Vorholzer, M., Vilhena, J.G., Perez, R., Gnecco, E., Dietzel, D., Schirmeisen, A.: Temperature activates contact aging in silica nanocontacts. Phys. Rev. X. 91, 041045 (2019).

171. Jiang, Y., Grierson, D.S., Turner, K.T.: Flat punch adhesion: transition from fracture-based to strength-limited pull-off. J. Phys. D. Appl. Phys. 47, 325301 (2014).

172. Persson, B.N.J.: Nanoadhesion. Wear. 254, 832–834 (2003).